

**Experimental Investigations of the Onset of Sand Deposits on Hastelloy-X between 1000 °C
and 1100 °C**

John Patrick Hutchinson

Thesis submitted to the faculty of the Virginia Polytechnic Institute and State University in
partial fulfillment of the requirements for the degree of

Masters of Science
In
Mechanical Engineering

Wing F. Ng
Srinath V. Ekkad
Kevin T. Lowe

October 10, 2016
Blacksburg, Virginia, USA

Keywords: Sand, Microparticle, Arizona Road Dust, Deposition

Copyright 2016

Experimental Investigation of the Onset of Sand Deposits on Hastelloy-X between 1000 °C and 1100 °C

John Patrick Hutchinson

ACADEMIC ABSTRACT

In many arid regions, particle ingestion can occur within propulsive gas turbines. The ingested particles can severely impact performance and may damage many primary gas path components through erosion or deposition. Characterizing crystalline deposits on metallic substrates can allow for the prediction of deposition to improve component resilience and develop health monitoring algorithms. This work investigates the effect of temperature and angle on sand deposits and attempts to quantitatively characterize the deposition of Arizona Test Dust (ATD) onto Hastelloy-X.

The first study presented in this thesis describes a preliminary investigation of sand deposition at temperatures and velocities similar to those found in the turbine section of propulsive gas turbine engines and presents an equation for predicting deposition as a function of gas path temperature and impact angle. The sand and air mixture maintained a constant flow velocity of approximately 70 m/s, impact angle was varied from 30° to 90°, and the gas path temperature was varied from 1000 °C to 1100 °C. The number of deposits was found to linearly increase with temperature for all coupon angles tested. The model was able to explain approximately 67% of the deposition that occurs, with the remaining percentage due to other factors such as injection rates and surface temperature.

The second study describes an improved investigation of sand deposition and presents an equation for predicting deposition as a function of surface temperature and impact angle. This study characterizes deposition using percent coverage in addition to deposits per square millimeter. Deposition is a quadratic function of both near surface coupon temperature and coupon angle. The model using deposits per mm² was able to explain 96.3% of the deposition that occurred and the model using percent coverage was able to explain 98.9% of the deposition that occurred.

Experimental Investigation of the Onset of Sand Deposits on Hastelloy-X between 1000 °C and 1100 °C

John Patrick Hutchinson

PUBLIC ABSTRACT

In desert regions, sand particles can be sucked into helicopter and airplane jet engines which can severely impact performance and may damage many engine components through erosion or hot deposits. By measuring the sticking properties of sand on materials used in jet engines, equations to predict sticking can be created and combined with previous erosion research to develop computational simulations of sand behavior in jet engines.

This work investigates the effect of temperature and angle on sand deposits and numerically characterizes the deposition of sand particles onto jet engine materials. The first study presented in this thesis describes an initial investigation of sand deposition at temperatures and speeds similar to those found in the turbine section of jet engines and presents an equation for predicting deposition as a function of flow temperature and impact angle. The model was able to explain approximately 67% of the deposition that occurs, with the remaining percentage due to other factors such as injection rates and test coupon surface temperature. The second study describes an improved investigation of sand deposition and presents an equation for predicting deposition as a function of metal surface temperature and impact angle. The model is able to explain 98.9% of the deposition that occurred.

The improved sand sticking model will allow designers to improve engine resilience and develop health monitoring algorithms. Improved resilience and health monitoring will increase airplane safety as well as reducing maintenance and operating costs when flying in sandy or arid regions.

Acknowledgements

I would first like to thank Andrew Boulanger, my co-researcher on this project. Without the long hours and tireless work he put into this experiment, this work would not have been possible. Thanks also to Matt Keefe, Weibin Xu, and William DeShong from the Virginia Tech Laboratory of Independent Statistical Analysis for assistance with experimental design, statistical analysis, and interpreting results.

Thank you to my co-advisors, Dr. Wing Ng and Dr. Srinath Ekkad, for the opportunity to work on this project. Working with you has been an honor and a privilege and I thank you for the guidance and direction you provided when problems were encountered. Thank you also to my other committee member, Dr. Todd Lowe, for being a resource on laser systems. I would like to thank all of the previous researchers on this project, who worked to getting the test rig working properly, including Hardik Patel, Jacob Delimont, and Colin Reagal. Also thanks to the shop staff Johnny, Bill, James, Phil, and Tim for their advice and help on machining and welding jobs. A very special thank you goes to Diana Israel for her assistance with placing orders, purchasing equipment, and reserving rooms.

I would like to thank Rolls Royce for sponsoring this project and donating the hardware used for the test rig. I would like to specifically thank Brett Barker, Kwen Hsu, Paul Davis, and Bruce Varney for their insights and support that helped advance the experiment.

Finally, I would like to thank my friends and family for their love and support, especially my mom Polly who never stopped encouraging me even when facing her own challenges.

Table of Contents

Preface	1
1. Paper #1: Preliminary Experimental Investigation of Initial Onset of Sand Deposition in the Turbine Section of Gas Turbines	4
1.1. Abstract	4
1.2. Nomenclature	5
1.3. Introduction	5
1.4. Background	6
1.5. Experimental Method	9
1.5.1. Aerothermal Rig	9
1.5.2. Testing Conditions	12
1.5.3. Statistical Modeling Method	14
1.6. Results	16
1.6.1. Raw Data	16
1.6.2. Statistical Model	21
1.7. Conclusions	24
Acknowledgments	25
References	25
2. Paper #2: Experimental Investigation of the Onset of Sand Deposits on Hastelloy-X between 1000 °C and 1100 °C	28
2.1. Abstract	28
2.2. Nomenclature	28
2.2.1. Symbols	28
2.3. Introduction	29
2.4. Experiment Method	30
2.4.1. Virginia Tech Aerothermal Rig	31

2.5.	Experiment Testing Conditions	33
2.5.1.	Statistical Modelling Method	36
2.6.	Results and Analysis	36
2.6.1.	Data Acquisition and Reduction	37
2.6.2.	Raw Data	38
2.6.3.	Statistical Models for Prediction	41
2.7.	Conclusion	42
	Acknowledgments	43
	References	43
3.	Conclusion and Future Work	46
	Appendix A: Modifications to the Virginia Tech Aerothermal Rig	48
A.1.	Sand Injector	48
A.2.	Fuel System	51
A.3.	Exhaust Quenching	53
A.4.	Camera/Laser Containment	54
A.5.	Rig Controls	55
	Appendix B: Data Reduction Code	58
B.1.	Data Reduction Block Diagram	59
B.2.	Particle_Counter_v18_rev2	60
	Appendix C: Non-Dimensionalization	67
C.1.	Theoretical Model	69

List of Figures

Figure 1-1: Comparison of the grains of Arizona Test Dust (LEFT) and MIL-5007C dust (RIGHT) [22]..... 8

Figure 1-2: Current setup of the Virginia Tech Aerothermal Rig (VTAR) for deposition testing up to 1100 °C. 10

Figure 1-3: A CAD representation of the coupon test arrangement..... 11

Figure 1-4: Two views of the test coupon arrangement. (LEFT) Top-down view of coupon and equilibration tube with the test section casing and flanges hidden. (RIGHT) An isometric view of the coupon and equilibration tube indicating thermocouple placement top and bottom of the coupon. The dashed line across the coupon surface indicates the horizontal midline of the coupon and gas flow path. 11

Figure 1-5: A baseline pre-test image of the coupon surface (LEFT) and a post-test microscopic image at 20x magnification from an 1100 °C and 80° coupon angle test condition. 17

Figure 1-6: Raw data (points), regression lines, and prediction intervals (shaded regions) for conditions between 975 °C and 1100 °C gas path temperatures for all tested angles. 19

Figure 1-7: Contour plot of the MLR model showing the expected number of particles per area based on average injection temperature and coupon angle..... 20

Figure 1-8: (LEFT) A distribution of the average particles per area does not follow a normal distribution and is skewed right. (RIGHT) The distributions of a square root of the average particles follows a normal distribution. 23

Figure 2-1: The Virginia Tech Aerothermal Rig (VTAR) utilized for deposition testing between 1000 °C and 1100 °C, highlighting the test section cut-away view and the associated coupon. 31

Figure 2-2: Two views of the coupon arrangement. (LEFT) Top-down view of coupon and equilibration tube with the test section casing and flanges hidden. (RIGHT) An isometric view of the coupon and equilibration tube indicating thermocouple placement top and bottom of the coupon. The yellow dashed line across the coupon surface indicates the horizontal midline of the coupon and gas flow path. 33

Figure 2-3: (LEFT) Pre-test and post-test surface sample image comparison showing the deposits and Hastelloy-X surface. The image size is 698 μm by 522 μm at 20x magnification. (RIGHT) Rendered image of the coupon surface that highlights the locations of the sample image rows

that are located at the midline, and the quarter and three quarter locations vertically along the horizontal axis.....	37
Figure 2-4: (LEFT) Average particle deposits per square millimeter on the coupon and (RIGHT) average deposit percent coverage area on the coupon. Both responses are plotted against near-surface coupon temperature. The average deposits per square millimeter is less than anticipated due to significant deposited particles overlapping on the surface.....	40
Figure 2-5: Particle deposits per area for the 50° and 80° coupon angle test cases with an estimated interval using the coverage area data.....	41
Figure A-1: Previous sand injection system with important components labeled.....	49
Figure A-2: New sand injection system with important components labeled.....	50
Figure A-3: A block diagram illustrating the operation of the sand injection system.....	51
Figure A-4: New fuel control system with important components labeled.....	53
Figure A-5: New camera/laser containment system (cooling hoses removed).....	55
Figure A-6: Front panel of the Aerothermal Rig control software. Controls are organized by Burner, Equilibration Tube, and Test Section.....	56

List of Tables

Table 1-1: Chemical analysis for typical Arizona Test Dust products from Powder Technologies Inc. 9

Table 1-2: Constant test conditions for varying gas path temperature and coupon angle testing. 13

Table 1-3: Testing matrix for varying gas path temperature bins and coupon angle. 16

Table 1-4: Deposits and achieved temperatures during testing for all testing conditions..... 18

Table 1-5: Multiple linear regression (MLR) model parameters using test data input into JMP®. 23

Table 2-1: Constant test conditions for varying flow temperature and coupon angle testing..... 34

Table 2-2: Aggregated deposit data for each test as well as the average near-surface temperature. 39

Table 2-3: R-squared and adjusted R-squared values for particle deposits per area (Equation 2-1) and deposit percent coverage (Equation 2-2)..... 42

Table C-1: Measured variables and other important constants along with their respective symbol and fundamental units 67

Preface

This thesis is written in manuscript format and contains two papers directly related to the Master's thesis. Although the author is not the first author on the papers included, he was directly involved in all aspects of the experiments described including planning, setup, testing, post-processing and analysis and wrote parts of the final papers. Other details of the work not discussed in the main body of the thesis can be found in the appendix.

A variety of methods have been used to measure deposition in propulsive gas turbine engines with much of the original work performed by Dunn [1]–[5]. These experiments involved both full scale and component testing of actual turbines. The results of these experiments are largely empirical as there is no method to directly characterize sand deposits, instead focusing on deposit locations, failure methods, and operational life. Full scale testing is important to determine the effect of particle ingestion on propulsion turbines, but improving the resilience of the engines requires an additional understanding of the basic deposition mechanisms. More recently, Bons has examined deposition in land based gas turbines for multiple particulates, but these studies analyze the long term buildup of deposition and do not address the deposition of sand [6,7]. Delimont analyzed the onset of particle deposition as part of a study of microparticle rebound characteristics and directly measured deposition using microscopic imaging [8]. The primary focus of the research presented in this paper is the initial onset of particle deposits building on that work.

The first study [9] primarily describes a method for quantifying the effect of various conditions on the onset of deposition. This paper was published in conference format at the ASME-International Gas Turbine Institute (IGTI) Turbo Expo 2016. Impact angle and gas path temperature were used as the predictors for deposition, which was measured by the number of deposited particles per mm^2 on a flat metal plate. An equation for predicting deposition of 20 to 40 μm Arizona Test Dust (ATD) onto Hastelloy-X as a function of gas path temperature and impact angle is presented in this paper.

The second chapter of this thesis is a paper [10] which describes an improved investigation of sand deposition. The paper has been submitted to the Royal Aeronautical Society (RAeS) Aero Journal Special Issue for 2016 and the International Society for Air Breathing Engines (ISABE) International Conference on Airbreathing Engines 2017. This study characterizes deposition using percent coverage in addition to deposited particles per square millimeter to address issues relating to excessive particle overlap on the coupon surface. This experiment characterizes deposits based

on surface temperature rather than gas temperature, as surface temperature was found to have a more direct role in deposition. The model using deposits per square millimeter was able to explain 96.3% of the deposition that occurred and the model using percent coverage was able to explain 98.9% of the deposition that occurred, a significant improvement over the previous study.

The initial deposition of sand particles was found to follow a quadratic function of both near surface coupon temperature and coupon angle, with an additional term for interaction between angle and temperature. The results of these experiments are a significant improvement in the understanding of deposition onto hot metal components. Since the studies directly characterize particle deposition rather than mass or thickness, the models can be applied to validate computational models of sticking probability or directly predict deposition in order to create designs resistant to sand deposition.

- [1] M. G. Dunn, C. Padova, and M. R. Adams, "Operation of Gas Turbine Engines in Dust-Laden Environments." Buffalo, p. 16, 1987.
- [2] M. G. Dunn, C. Padova, J. E. Moller, and R. M. Adams, "Performance Deterioration of a Turbofan and a Turbojet Engine Upon Exposure to a Dust Environment," *J. Eng. Gas Turbines Power*, vol. 109, no. 3, pp. 336–343, 1987.
- [3] M. G. Dunn, "Exposure of Air Breathing Engines to Nuclear Dust Environment (U)," p. 120, 1991.
- [4] M. G. Dunn, A. J. Baran, and J. Miatech, "Operation of Gas Turbine Engines in Volcanic Ash Clouds," *J. Eng. Gas Turbines Power*, vol. 118, no. October, pp. 724–731, 1996.
- [5] M. G. Dunn, "Operation of Gas Turbine Engines in an Environment Contaminated With Volcanic Ash," *J. Turbomach.*, vol. 134, no. 5, p. 51001, 2012.
- [6] J. P. Bons, J. M. Crosby, J. E. Wammack, B. I. Bentley, and T. H. Fletcher, "High-Pressure Turbine Deposition in Land-Based Gas Turbines From Various Synfuels," *J. Eng. Gas Turbines Power*, vol. 129, no. 1, p. 135, 2007.
- [7] J. E. Wammack, J. Crosby, D. Fletcher, J. P. Bons, and T. H. Fletcher, "Evolution of Surface Deposits on a High-Pressure Turbine Blade—Part I: Physical Characteristics," *J. Turbomach.*, vol. 130, no. 2, p. 21020, 2008.
- [8] J. M. Delimont, W. F. Ng, S. V Ekkad, D. K. Tafti, T. Lowe, and G. R. Pickrell, "Experimental Investigation of Temperature Effects on Microparticle Sand Rebound

- Characteristics at Gas Turbine Representative Conditions,” p. 186, 2014.
- [9] A. Boulanger, H. Patel, J. Hutchinson, W. Deshong, and W. Xu, “Preliminary Experimental Investigation of Initial Onset of Sand Deposition in the Turbine Section of Gas Turbines,” in *ASME Turbo Expo 2016*, 2016, pp. 1–10.
- [10] A. Boulanger, J. Hutchinson, W. Ng, S. Ekkad, M. Keefe, and Xu, “Experimental Investigation of the Onset of Sand Deposits on Hastelloy-X between 1000 ° C and 1100 ° C,” 2017.

1. Paper #1: Preliminary Experimental Investigation of Initial Onset of Sand Deposition in the Turbine Section of Gas Turbines

1.1. Abstract

Particle ingestion into modern gas turbine engines is known to reduce performance and may damage many primary gas path components through erosion or deposition mechanisms. Many studies have been conducted that evaluate the effects of particulate ingestion in primary and secondary gas path components. However, modern gas turbines have gas path temperatures that are above most previous studies. As a result, this study performed particle deposition experiments at the Virginia Tech Aerothermal Rig facility at engine representative temperatures. Arizona Test Dust of 20 to 40 μm was chosen to represent the particle ingested into rotorcraft turbine engines in desert and sandy environments. The experimental setup impinged air and sand particles on a flat Hastelloy-X coupon. The gas and sand mixture impacted the coupon at varying angles measured between the gas flow direction and coupon face, hereby referred to as coupon angle. For this study, gas and sand particles maintained a constant flow velocity of about 70 m/s and a temperature of about 1100°C. The coupon angle was varied between 30° to 90° for all experiments. The experimental results indicate sand deposition increased linearly from about 975 °C to 1075 °C for all coupon angles. A multiple linear regression model is used to estimate the amount of deposition that will occur on the test coupon as a function of gas path temperature and coupon angle. The model is adequate in explaining about 67% of the deposition that occurs for the tests. The remaining percentage could be explained with other factors such as particle injection rates and exact surface temperature where the deposits occur.

1.2. Nomenclature

ATD	Arizona Test Dust
CAD	Computer-aided Design
MLR	Multiple Linear Regression
PIV	Particle Image Velocimetry
PPMW	Parts Per Million by Weight
VTAR	Virginia Tech Aerothermal Rig
β_0	Intercept Parameter
β_T	Temperature Parameter
β_θ	Coupon Angle Parameter
$D_{T,\theta}$	Estimated Deposits per Area
ε	Random error
T	Gas Path Temperature ($^{\circ}\text{C}$)
θ	Coupon Angle (degrees)

1.3. Introduction

Operation of propulsion turbines in dust-laden environments is known to reduce performance and cause damage to various system components. Ingested particles will enter the primary gas paths where they can erode metal surfaces and entrain the coolant bypass system in the compressor section. The particulates will continue into the combustor and turbine sections where they could melt and deposit on the various hot section parts. The deposits may lead to overheating and melting of substrate material from clogged film cooling holes.

This study focuses on the initial onset of microparticle deposition at representative gas turbine hot-section temperatures. Specifically, this work follows the high temperature microparticle rebounding experiments and modeling previously performed at Virginia Tech [1–7]. The purpose is to determine a statistical estimate of the initial onset of deposition for 20 to 40 μm Arizona Test Dust (ATD) as a function of gas path temperature and relative microparticle impact angle. The experiments were performed at the near melting point of the ATD on an uncooled flat Hastelloy-X test coupon. Deposition in this study is quantified by counting particles per area on multiple microscopic images on the coupon surface. Quantifying the onset of deposition at engine-representative temperatures is important to estimate subsequent deposits in hot-section gas turbine conditions.

1.4. Background

Particulate ingestion into propulsion turbines is a common event in many arid regions across the world. The detrimental effects of particulate ingestion can vary depending on a variety of factors, including mass ingested, particulate composition, engine material properties, etc. Increasing service interval frequency is a common way to mitigate particulate ingestion for propulsion turbines. In more severe cases, the engines can be catastrophically damaged. For instance, during the Mount St. Helens eruption, an L-100 aircraft had two engines fail while the other two had partial power loss while flying below the ash cloud after the eruption began [8]. The observed damage to the engines was severe abrasion of the compressor section as well as melted dust in the turbine section of all the engines. Another example was during Operation Desert Shield and Desert Storm in 1991, where several M1 Abrams tank turbines failed due to sand ingestion [9]. A recent example on May 17, 2015, an MV 22 Osprey crashed in dusty conditions during a training exercise in Hawaii. Currently, the exact cause of this crash is unknown, but dust ingestion may have been a factor [10].

Particulate ingestion effects have been previously studied to determine the performance degradation and resilience on common propulsion turbine engines. A catalyst for some of the early studies was the aforementioned eruption of Mount St. Helens and the dust cloud effects on the L-100 aircraft engines. Additionally, the detonation of nuclear weapons can loft dust into the atmosphere where it would be ingested by aircraft engines and subsequently cause engine damage [8]. As a result, a T33 turbofan and J75 turbojet were tested in dust-laden environments to evaluate performance degradation and damage. The dominant damage to the test engines was compressor blade erosion, but there were no glassy deposits found on the hot section components unlike the aforementioned L-100 aircraft [11–13]. Subsequent testing of an F-100 turbofan engine in a simulated nuclear dust environment was intended to extend the operational life of an engine that had been severely damaged due to particle ingestion. The F-100 turbofan experienced damage mechanisms of erosion and deposition in the cold and hot sections of the engine, respectively. The operators of those tests were able to “clean” the engine by rapidly cycling the power levels, inducing thermal transient in the turbine airfoils. The thermal transient caused the deposited material to break free of the internal turbine substrates. However, after a long exposure to various particulates and feed rates, the engine was damaged beyond operational capability [14].

Full scale testing is important in addressing propulsion turbines responses and endurance to particulate ingestion. Improving the resilience of the engines requires an additional understanding of the basic erosion and deposition mechanisms on the individual components. The primary focus of the research presented in this paper is the onset of particle deposits. The erosion mechanisms will not be discussed in extensive detail.

Subsequent experiments after the F-100 full engine tests involved testing deposition on a nozzle guide vane (NGV) cascade one quarter section with various cooling schemes and different dust blends. The general conclusion from the testing is that deposition of particulates onto the NGVs is dependent on the particulate type and size as well as the substrate surface temperature [15]. Subsequent testing of cylinders and cascade sections confirmed that substrate surface temperature and particulate type does dictate deposit build up. In addition, large thermal gradients and thermal cycling of the substrate may result in removal of the deposits [16].

Since dust and sand can vary in composition and size. Testing has been performed on various airframes to determine the quantity and sizing of sand occurs in brownout conditions [17]. Typical dust concentrations in extreme conditions (depending on airframe) can be as high as 5000 parts per million by weight (PPMW), which can be ingested into the engines. Dust composition can vary depending on geographic location. For instance, even in a relatively small region in the Dhahran area the composition of sand is primarily SiO₂ and Al₂O₃ but can vary in large proportions [18,19]. The large variation in sand composition will affect the deposition characteristics in the hot sections of the turbine. Typically, the glassy-deposits in the hot sections are referred to as CMAS since they are a composition of calcium, magnesium, aluminum, and silicon oxides.

The deposition of particulate is dependent on the motion mechanisms and the particle material phase as a function of temperature. The motion mechanisms of deposition are inertial impaction, turbulent diffusion/eddy impaction, Brownian diffusion, and thermophoresis [20]. Previous testing and modeling has generally demonstrated deposition as a function of particulate size. Above 1 μm , the particulate deposit mechanism is dominated by inertial impacts. Since this study utilizes ATD of 20 to 40 μm , the primary mechanism is inertial impaction for all tests. The particle temperature and phase of the material can determine the probability that a particle will stick to a substrate when coupled with particle motion. The particulate material at elevated temperatures will proceed through four phases as temperature increases. The four phases are characterized as the shrinking temperature, deformation temperature, hemisphere temperature, and flow temperature [21]. Each

phase temperature can vary depending on the particulate and all four phases occur during the sintering phase. Additionally, as the temperature increases, the probability of deposition increases since the particulate material is effectively “softened”.

For this study, the particulate used for deposition testing is ATD from Powder Technologies Inc. The typical chemical composition, shown in *Table 1-1*, indicates that silicon and aluminum oxides are the primary constituents. ATD has an onset sintering temperature of 1100°C for sizing less than 63 μm [22]. The sintering temperature indicates the beginning of the softening temperature of the ATD particulate. In the high temperature environments, such as the hot sections of a gas turbine, typical ATD will lose 2-5% of its original sample mass due to the water in the particulate samples evaporating from ambient temperature to 700°C. The shape of ATD is more angular than MIL-5007C test dust, which is primarily composed of quartz. The shape and sintering temperature phases of the particulate will affect deposition on hot turbine components. For this study the particulate shape and impact orientation is not evaluated. The deposition investigated is primarily a function of gas path and environmental temperatures.

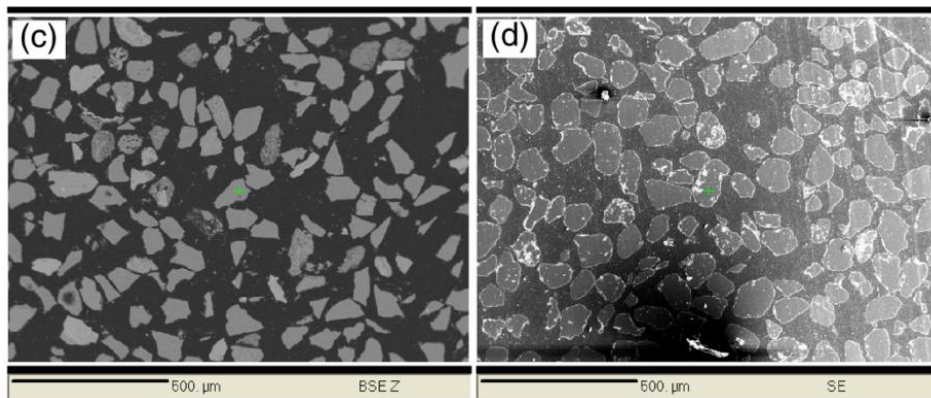


Figure 1-1: Comparison of the grains of Arizona Test Dust (LEFT) and MIL-5007C dust (RIGHT) [22].

Table 1-1: Chemical analysis for typical Arizona Test Dust products from Powder Technologies Inc.

Component	Percentage by Weight
SiO ₂	68-76%
Al ₂ O ₃	10-15%
Fe ₂ O ₃	2-5%
Na ₂ O	2-4%
CaO	2-5%
MgO	1-2%
TiO ₂	0.5-1.0%
K ₂ O	2-5%

1.5. Experimental Method

1.5.1. Aerothermal Rig

The Virginia Tech Aerothermal Rig (VTAR) was donated by Rolls Royce (Indianapolis, IN) to Virginia Tech in 2010. The previous application of the rig prior to the donation was for heat transfer studies of cascade turbine airfoils [23–26]. The VT Aerothermal Rig was used to conduct all the experiments discussed in this paper.

Figure 1-2 is a schematic CAD model of VTAR’s current configuration for sand deposition testing. VTAR was used for erosion based testing by evaluating the coefficient of restitution (COR) [1–7]. Since the previous work performed at Virginia Tech [6], the fuel source was changed from methane to propane and the maximum gas path temperature at the test coupon has been increased to about 1100 °C. In addition, the focus of the analysis has shifted from COR to deposition using ATD. The main gas path mass flow rate is about 0.1 to 0.15 kg/s depending on testing temperature. The equilibration tube is 7.62 cm in diameter and 1.82 m long. The flow velocity leaving the equilibration tube is maintained to 70 ± 2 m/s.

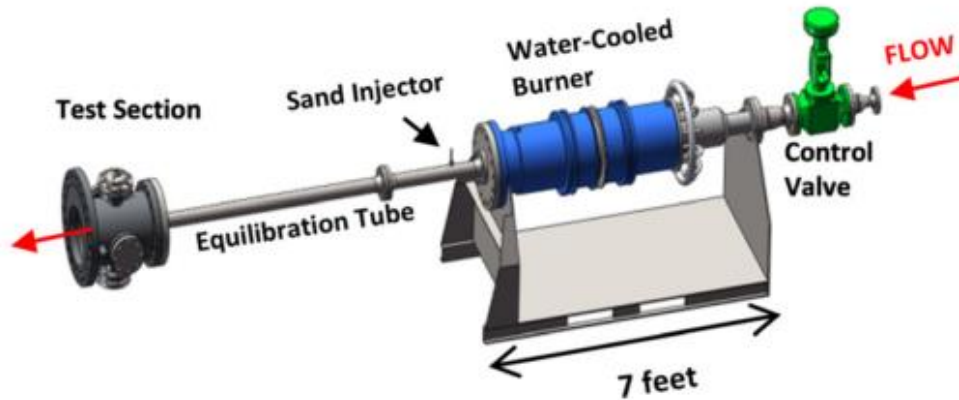


Figure 1-2: Current setup of the Virginia Tech Aerothermal Rig (VTAR) for deposition testing up to 1100 °C.

The sand particles are entrained in a flow separate from the main flow and are injected into the main flow in the equilibration tube after the burner. The sand is drawn from a hopper using a venturi style entrainment system. The sand laden flow is then injected into the main gas path in the upstream direction to promote sufficient mixing by the end of the equilibration tube. The equilibration tube length allows a sufficient amount of time for the temperature of the sand particles to equalize with the gas path temperature.

Figure 1-3 is a CAD representation of the test coupon support system inside the test section (with the outer case wall hidden). The coupon can be rotated in 10° increments. The coupon angle is defined as the acute angle between the gas path and the surface of the coupon, Figure 1-4 (left). Gas path flow temperature measurements are taken with two thermocouples placed above and below the coupon and within the gas path, Figure 1-4 (right). The distance from the end of the equilibration tube to the leading edge of the coupon is approximately 10 cm. The distance will change during operations due to the thermal expansion of the tube into the test section via a slip joint. The coupon material is Hastelloy-X, which is the same from the previous study [6].

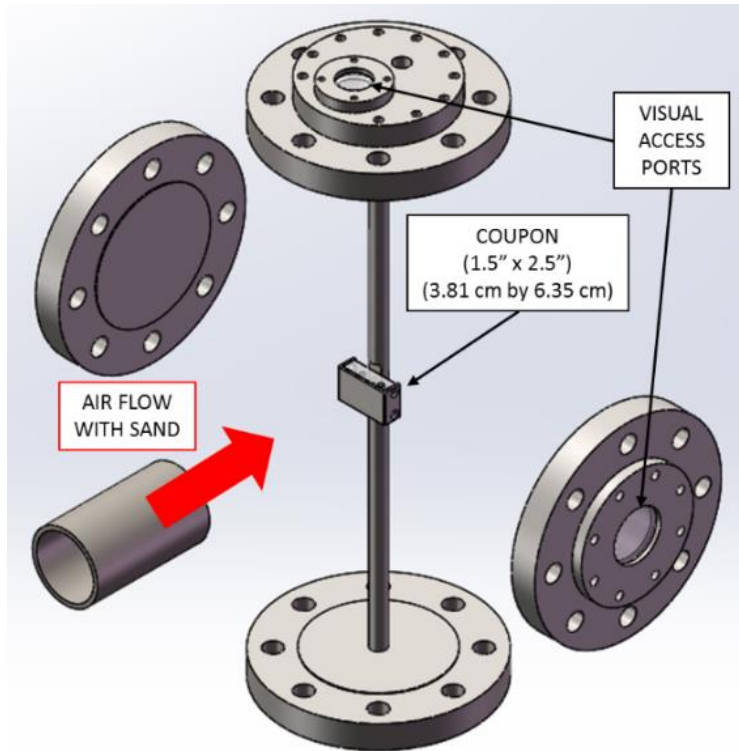


Figure 1-3: A CAD representation of the coupon test arrangement.

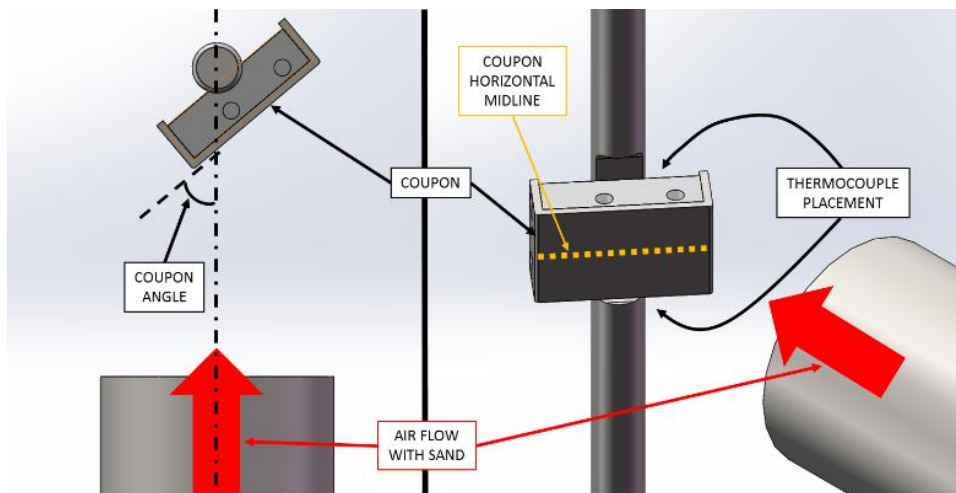


Figure 1-4: Two views of the test coupon arrangement. (LEFT) Top-down view of coupon and equilibration tube with the test section casing and flanges hidden. (RIGHT) An isometric view of the coupon and equilibration tube indicating thermocouple placement top and bottom of the coupon. The dashed line across the coupon surface indicates the horizontal midline of the coupon and gas flow path.

1.5.2. Testing Conditions

Table 1-2 is a summary of the microparticle deposition testing conditions for this study. The particulate used is 20 to 40 μm ATD and the gas path flow velocity is 70 m/s to maintain consistency from the previous studies using VTAR [1–7]. The ATD used for all testing maintains the same relative ISO distribution from *Table 1-1*. The authors are aware that ATD is not a practical representation for deposition studies compared to airborne sands and dusts found across the world [11]. Additionally, the particulate sizing is not directly representative of sand sizing in the hot section of turbine engines. Particle sizing is typically below 10 μm after the cold sections of a turbine engine since the particles are “pulverized” as they travel through the compressor. For example, testing of TF33 turbofan and J57 turbojet engines had a mean particulate size after the compressor of 6 μm [13]. Particles larger than a few microns in diameter are dominated by inertia impaction mechanisms for deposition. Alternate mechanisms of deposition such as turbulent diffusion and thermophoresis dominate particles under a few microns in size [20]. Based on particle deposition mechanism sizing from earlier studies, 20 to 40 μm the ATD size is relevant for inertial impact deposition mechanisms. In addition, the ATD used for this study provides continuity with the earlier deposition study at Virginia Tech [6] as well as improves the detection of deposited particles using an image processing computer software.

VTAR’s sand injection system is maintained from the previous COR and deposition studies [6,7]. Before each test, the coupon is polished to a mirror finish with a measured root mean square roughness of less than 0.2 μm to ensure roughness effects are minimized. Dust concentrations ingested by turbine engines on airframes can be as high as 5,000 PPMW for extreme low visibility conditions [17]. Microparticle injection rates for VTAR can vary between 1 to 2 grams per second. All the ATD sample is injected between 5 to 10 seconds, which correlates to approximately 10,000 to 20,000 PPMW of ATD equivalent being injected into the equilibration tube where the particles reach the flow temperature and velocity and subsequently impact the test coupon. The total sand injected per test was maintained at a constant 10 grams. Preliminary testing established the relatively low total sand loading to minimize deposits from being inadvertently removed from the surface through subsequent impacts.

Table 1-2: Constant test conditions for varying gas path temperature and coupon angle testing.

Particulate Type/Size	ATD, 20 – 40 μm
Bulk Flow Velocity	70 ± 2 m/s
Desired Gas Path Temperature Range	1000 $^{\circ}\text{C}$ to 1100 $^{\circ}\text{C}$
Injection Rate	~ 1 g/s to 2 g/s
Total Sand Loading	10 grams
Coupon Angles	30 $^{\circ}$, 50 $^{\circ}$, 80 $^{\circ}$, 90 $^{\circ}$
Coupon Material	Hastelloy-X
Coupon Surface Roughness	≤ 0.2 μm
Coupon Thickness	3.175 mm
Particle Stokes Number	~ 1.6 (20 μm) to 6.8 (40 μm)

Unlike the constant coupon angles, the gas path temperatures can vary during ATD injection. Before injection, the gas path temperatures are maintained to within 5 $^{\circ}\text{C}$ of the target testing main gas path temperature. After all testing parameters are at steady state, the ATD is injected. Since air and sand is being added to the gas path, the average gas path temperature drops, typically, 10 $^{\circ}\text{C}$. During the injection transient, the temperatures are recorded and averaged. For example, a target temperature would be 1000 $^{\circ}\text{C}$, but during injection the average gas path temperature drops to 980 $^{\circ}\text{C}$. Since the temperatures are near and/or above the sintering or melting temperature of ATD [22], slight changes in temperature have a large impact on the overall deposition.

Substrate and surface temperatures of test pieces are directly linked to large scale deposit testing. In the previous study [6], the test coupons were assumed to be under an isothermal condition with a surface temperature approximately 140 $^{\circ}\text{C}$ below the gas path temperature. In this study, the surface temperature assumption is not maintained. Due to test equipment constraints, coupon surface temperature could not be directly measured. However, the surface temperature is a relative function of the gas path temperature and heat transfer to the coupon support structure and the surrounding walls in the test section.

Experimental relations for jet impingement onto a flat plate [27] are used to determine the convective heat transfer coefficient of the system and one-dimensional heat transfer calculations were performed to determine an estimate of the coupon surface temperature from conduction, convection, and radiation effects. From this analysis, it was found that coupon angle has little effect on the surface temperature and that the coupon surface temperature is within ± 2 $^{\circ}\text{C}$ of the

temperature measured on the back surface of coupon for all test cases. The coupon back temperatures are included in Table 1-4.

From testing prior to this study, glassy deposits developed inside a ceramic equilibration tube that began near the injection location and continued approximately half the length of the tube. Typically, ceramic substrates will collect and maintain deposits more readily than a metallic substrate during thermal cycling. The ceramic substrate and the sand particles will maintain their bond due to similar thermal expansion coefficients. For this study, the authors used a stainless steel equilibration tube instead of a ceramic tube. Negligible deposits were found during borescope inspections (every two to three tests). Deposits during sand injection were still anticipated but any significant deposits most likely delaminated from the inside surface of the tube and move downstream during cool down period of each test. Therefore, there is no significant flow change to main gas path during testing between tests.

Although there is no significant build up over time inside the equilibration tube, there is uncertainty associated with the deposition occurring inside the equilibration tube during that may reduce the sand reaching the coupon. Due to time constraints and resource limitations, the tube could not be weighed before and after each test. In addition, the relative added weight by any deposited sand would be negligible compared to the weight of the equilibration tube and hardware. Further study is necessary to quantify the deposits on parallel flow surfaces using ATD. However, the statistical method developed in this study helps mitigate the uncertainty of the equilibration tube deposition.

1.5.3. Statistical Modeling Method

Compared to the previous study at Virginia Tech [6], this study establishes a method for estimating the onset of deposition at various coupon angles and average gas path temperatures. A method to examine the effect of combinations of gas path temperature and coupon angle on the average sand deposition, i.e. if there is any difference in sand deposition among three target gas path temperatures (1000 °C, 1050 °C and 1100 °C) and among the four coupon angles (30°, 50°, 80° and 90°) is needed. Therefore, a two-way layout experimental design is used to study the effect of gas path temperature and coupon angle on deposition [28].

There are three levels of gas temperatures and four levels of coupon angles, leading to a total of 12 possible experimental conditions. In order to have enough degrees of freedom for the error

term [28] and to factor out the differences in sand deposition caused by random variation between experiments, replicate testing is necessary for each experimental condition. Ideally, more replicates reduce the effect of random variation on the response variable, deposition. However, due to the time and budget constraints, only two tests were conducted for each experimental condition. Therefore, the total number of tests performed is 24.

A statistical software, JMP®, generated the experimental condition testing order for a total of 24 tests that meets the four rules of a perfect two-way layout experimental design, Table 1-3. JMP® ensures that the experimental design for this study (1) is “randomized”, (2) has “fixed effects”, (3) is “completely balanced” and (4) “completely crossed” [29]. If all four rules are met, the effect of each factor on the response variable can be measured. In addition, the effect of each factor on the response variable and have more degrees of freedom and the power will be maximized for the statistical model. A “randomized” design requires that each ATD sample is randomly assigned to each experimental condition. This is achieved by randomizing the order of the experimental conditions. Randomizing the order reduces bias caused by uncontrollable factors during the testing of each experimental condition, such as the local air pressure and humidity during each test day. The “fixed effects” in this model are the gas path temperature and coupon angle, which means they are the primary variables of interest and not randomly generated. A “completely balanced” design assumes each factor is run the same amount of times in the experiment and equal weights for each treatment in the analysis of variance [29,30]. Lastly, “completely crossed” means that all the levels of gas path temperature and coupon angle are present for all the levels of one another, which results in the aforementioned total of 12 experimental conditions.

Table 1-3: Testing matrix for varying gas path temperature bins and coupon angle.

Index	Target Temperature (°C)	Coupon Angle (degrees)	Index	Target Temperature (°C)	Coupon Angle (degrees)
1	1000	90	13	1050	90
2	1000	80	14	1050	80
3	1100	50	15	1100	80
4	1100	30	16	1000	30
5	1100	30	17	1100	90
6	1000	50	18	1050	50
7	1050	90	19	1050	80
8	1000	50	20	1000	80
9	1100	50	21	1000	90
10	1000	30	22	1050	50
11	1100	80	23	1050	30
12	1050	30	24	1100	90

1.6. Results

1.6.1. Raw Data

Figure 1-5 is an example of a pre-test and post-test (1100 °C and 80° coupon angle) microscopic sample image at 20x magnification. Images are taken in series across the horizontal midline of the coupon starting from the leading edge and continuing towards the trailing edge, see Figure 1-4 (right). Images are taken in close proximity to each other but cannot be stitched together due to data acquisition equipment and processing limitations. The images are taken with the focus set to the coupon surface and the particles slightly out of focus resulting in a distinct boundary between the uniform particle and the non-uniform background. Each image is processed using the MATLAB® Visual Processing Toolbox to identify and trace the boundaries of each particle with a cross section corresponding to a circular diameter larger than 10 μm, to ensure most of the smaller particle deposits are counted. Due to the irregular shape of ATD particulate [22], the lower limit is assumed to be adequate for a majority of the deposited particles.

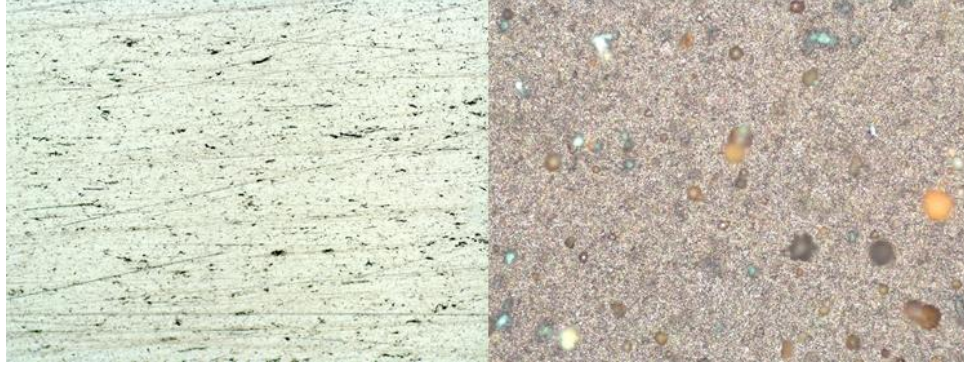


Figure 1-5: A baseline pre-test image of the coupon surface (LEFT) and a post-test microscopic image at 20x magnification from an 1100 °C and 80° coupon angle test condition.

Each image is then manually checked to ensure all particles have been successfully identified and no false positives have occurred. In addition, based on microscopic images, the particles do not appear to have delaminated from the coupon surface during or after post-test cooldown. The local adhesion between Hastelloy-X, a nickel-based substrate, and SiO₂, a primary constituent for ATD, creates a strong atomic level bond that is resistant to thermal cycling. Previous research has implied that a crystalline SiO₂ layer between a nickel substrate alloy and a thermal barrier coating could provide the bond strength necessary to avoid delamination during thermal cycling [31]. Since the bond between the nickel-based substrate and the SiO₂ is stronger than the rest of the crystalline structure of the SiO₂, the remaining crystal structure above the bonded region may fracture and liberate itself from the bonded layer. A bonded region with some crystalline structure should remain that can be counted with the image processing method described previously.

Overall, the deposition counts confirm the previous study's conclusion that deposition increased as primary gas path temperature increased from 950 °C to 1050 °C for all test coupon angles [6]. Table 1-4 is the raw data of deposits and achieved gas path and coupon temperatures for all testing conditions. The index for each condition correlates to Table 1-3. Under most conditions, the temperatures dropped below the target temperatures due to the injection of sand and air into the main gas path. The temperature drop is directly caused by the sand injection process. During the injection process, air at ambient temperature (20 °C to 30 °C) is injected into the main flow. The injection air contributes about 5% to 6% of the total gas mass flow rate.

Table 1-4: Deposits and achieved temperatures during testing for all testing conditions.

Index	Temperature (°C)			Coupon Angle (degrees)	Deposits Particles/mm ²
	Target	Achieved	Coupon Back		
1	1000	995	854	90	4
2	1000	1000	853	80	3
3	1100	1090	981	50	41
4	1100	1089	1064	30	104
5	1100	1076	1057	30	69
6	1000	988	952	50	12
7	1050	1012	924	90	67
8	1000	972	949	50	8
9	1100	1080	965	50	59
10	1000	982	903	30	0
11	1100	1092	934	80	120
12	1050	1012	937	30	20
13	1050	1008	925	90	73
14	1050	1013	916	80	84
15	1100	1067	948	80	120
16	1000	988	914	30	3
17	1100	1068	902	90	59
18	1050	1032	932	50	21
19	1050	1042	899	80	30
20	1000	989	870	80	10
21	1000	990	859	90	29
22	1050	1042	929	50	22
23	1050	1039	950	30	17
24	1100	1080	927	90	110

Figure 1-6 is the average particles per area for all the test conditions of average injection temperature and coupon angle. JMP® is able to develop regression trend lines for all the coupon angle conditions as well as 90% prediction intervals (shaded regions). For this study, the absolute test data and trend lines are used in the analysis. From the data, the deposition trends at certain coupon angles do not follow anticipated behavior. Some of the discrepancy can be attributed to testing conditions that are discussed later in this section. Figure 1-7 is a contour plot developed from the trend lines in Figure 1-6.

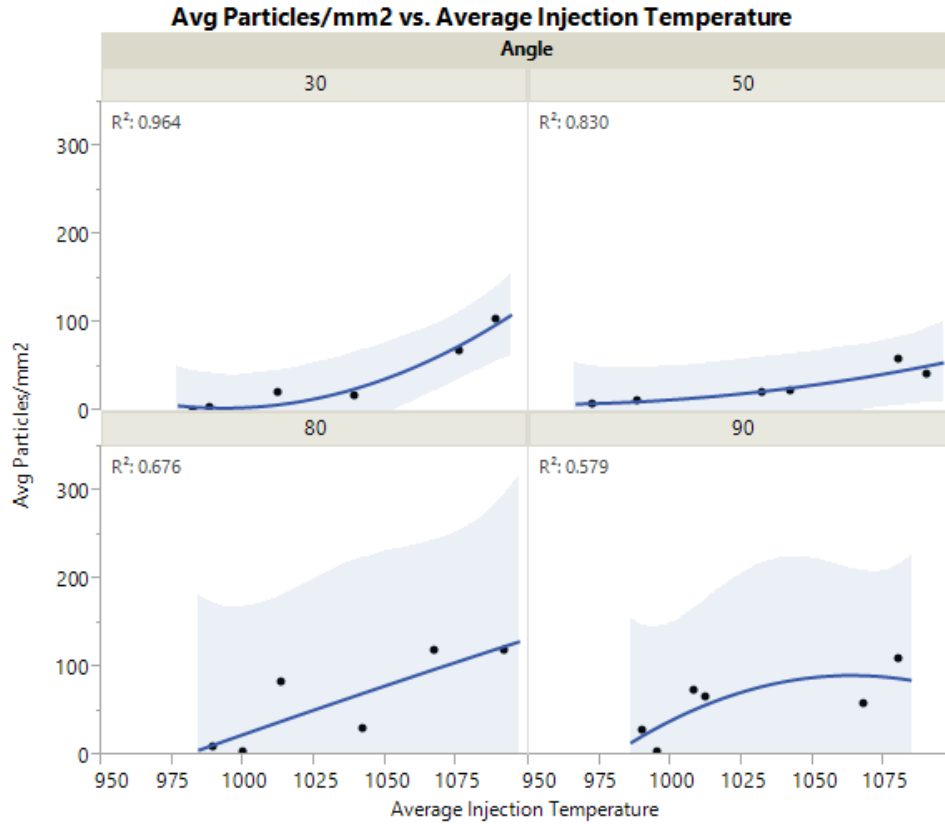


Figure 1-6: Raw data (points), regression lines, and prediction intervals (shaded regions) for conditions between 975 °C and 1100 °C gas path temperatures for all tested angles.

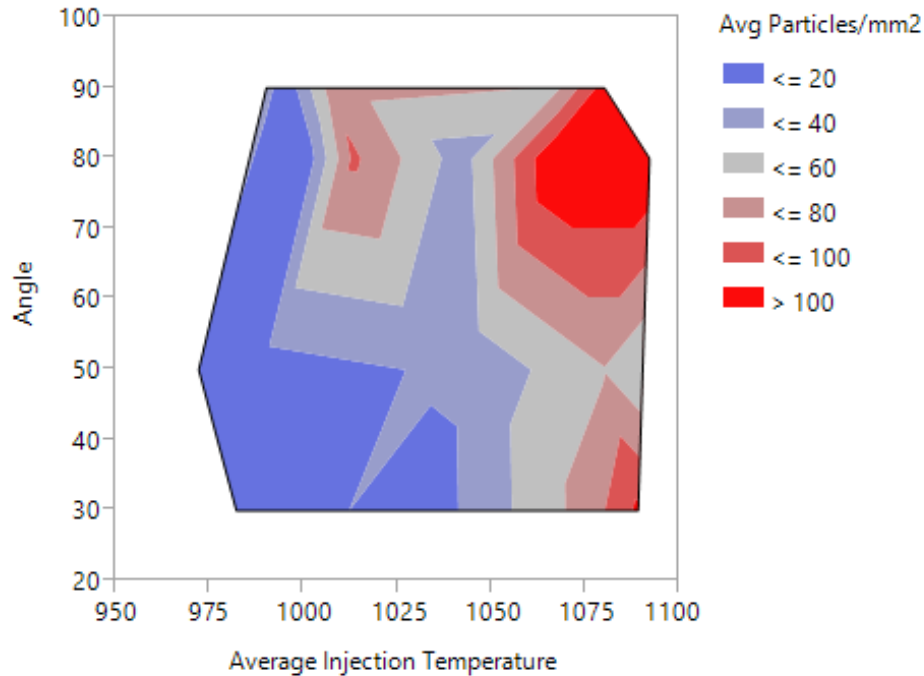


Figure 1-7: Contour plot of the MLR model showing the expected number of particles per are based on average injection temperature and coupon angle.

The melting point of ATD corresponds to when deposition is assumed to begin. Previous sintering tests on ATD showed that sintering begins for particles less than 63 μm around 1100 $^{\circ}\text{C}$ [25]. The deposition tests in this study use particles between 20 and 40 μm . One can extrapolate that smaller particles begin to soften and/or sinter at a lower temperature. In this case of testing, 20 to 40 μm ATD may start to soften around a gas path temperature of 1050 $^{\circ}\text{C}$. Based on the data in Figure 1-6, deposition generally appears to increase linearly from about 975 $^{\circ}\text{C}$ to 1075 $^{\circ}\text{C}$ except for the 30 $^{\circ}$ coupon angle case. However, the 30 $^{\circ}$ coupon angle case at higher testing temperatures is a potential outlier.

It is noted that several data points are outliers due to variations in testing conditions. The authors were unable to retest several data points due to resource constraints. For instance, the 30 $^{\circ}$ coupon angle case at higher temperatures (greater than 1075 $^{\circ}\text{C}$) has significantly more deposition than the 50 $^{\circ}$ cases at similar temperatures. The large amounts of deposition is most likely the result of gas path temperatures higher than those measured. The cause was determined by the authors to be a large displacement of the coupon outside of the main gas flow path in the test section for tests 1 through 8 due the thermal expansion of the support rod. For those tests, a secondary thermocouple below the coupon was not present due to prior operating processes and procedures.

After test 8, a closed circuit camera was added to the side viewing window of the test section to verify coupon placement in the gas path. During subsequent operation, the authors observed that the coupon was displacing the primary thermocouple outside of the main gas path flow. Since the thermocouple was displaced outside of the gas path flow at high temperatures, the recorded temperature was less than the centerline main gas path temperature. For the test cases greater than 1075 °C and 30° coupon angle, the estimated temperature is closer to 1200 °C since a majority the deposits had circular profiles, which indicates that the sand particles may have completely melted [22] just before impact with the coupon.

The feedback control system of VTAR for heat input depends on the temperature at the coupon. If the temperature is lower than indicated, additional heat is added to the main gas path flow until the desired temperature is achieved. For the remaining tests (9 through 24), a secondary thermocouple was placed below the coupon to ensure the coupon was centered in the main gas path flow. In addition, the mounting components for the test coupon were altered to minimize extreme displacement during tests. Unfortunately, repeating tests 1 through 8 was not feasible due to timeline and resource constraints. Utilizing the data from those tests is allowable due to the statistical model developed for this study. The statistical model in the following section still maintains a strong correlation between gas path temperature and coupon angle with deposited sand particles.

For the 90° coupon angle tests above 1075 °C, the reduced deposition may be attributed to a large stagnation area in front of the coupon. The highest deposition was anticipated at the highest temperature and highest coupon angle. A hypothesis is the stagnation area could reduce the Stokes number of the particles just ahead of the coupon and subsequently divert a large portion of the particles around the coupon. In addition, if the particles are slowed down in the test section which is cooler than the equilibration tube, the particles may solidify and bounce off the surface instead of adhering. Overall, variation in the experimental data are taken into account for the statistical model discussed in the following section.

1.6.2. Statistical Model

The typical analysis for a two way layout is a two-way Analysis of Variance (ANOVA). This analysis would give an estimate for each level of the factors tested assuming they are categorical. For example, the model is only capable of estimating the average deposition at 1000 °C and 30°

coupon angle or 1050 °C and 50° coupon angle. The model would not be capable of estimating the deposition at 1025 °C and 40° coupon angle. Therefore, a generic multiple linear regression (MLR) model his used instead.

The MLR model response is the average number of particles per area and the predictors are average gas path temperature during ATD injection and coupon angle. The major difference between the MLR model and the categorical model is that the predictors are now considered to be continuous. Therefore, a value for the average number of particles deposited can be calculated for gas path temperatures and coupon angles that were not directly tested.

The square root of the average sand particles deposited is the optimal MLR model developed using the JMP® modeling tools for this study. The square root transformation was chosen because it yields a response that follows an approximate normal distribution, Figure 1-8 (right). Alternative models were considered but do not provide the simplicity of a quadratic response to deposition for the two predictor variables tested. The MLR model has three primary requirements. First, the combined response (average deposition) of all sample data is assumed to have an approximately normal distribution. Since the sample average deposition data is not normally distributed, Figure 1-8 (left), a square root transform is conducted. Secondly, the MLR model assumes that there is a linear trend between the square root of average sand deposition and temperature and angle respectively (untransformed would have a quadratic trend). The last assumption is constant variance. All of these assumptions are met when the square root transformation is used.

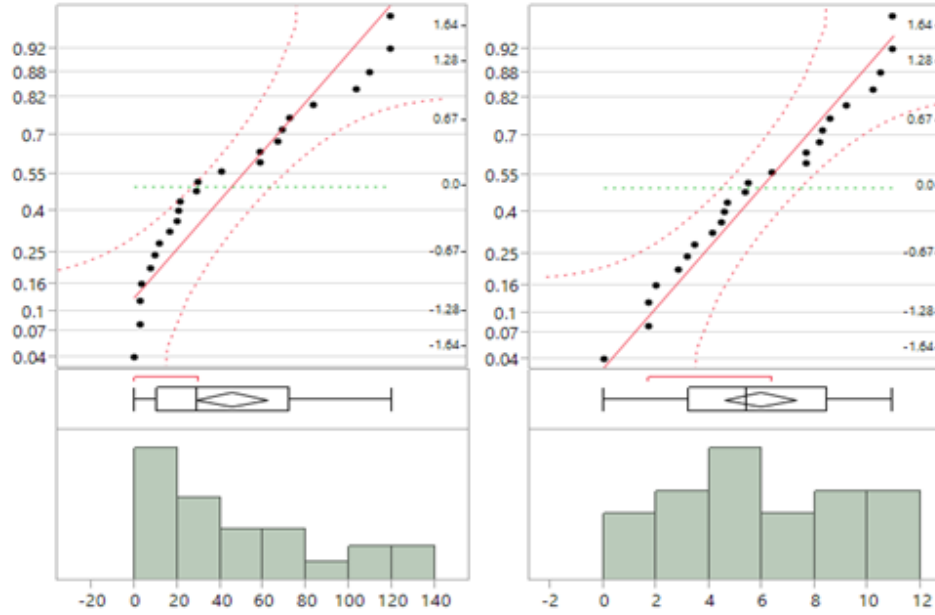


Figure 1-8: (LEFT) A distribution of the average particles per area does not follow a normal distribution and is skewed right. (RIGHT) The distributions of a square root of the average particles follows a normal distribution.

Equation (1-1) is the MLR model equation format developed for estimating deposition. Where $D_{T,\theta}$ is the average sand particles deposited per area, β_0 is the intercept, β_T is the temperature parameter, T is gas path flow temperature in Celsius, β_θ is the coupon angle parameter, θ is the coupon angle in degrees and ε is random error. Table 1-5 contains the parameters for the deposition model from JMP®. In addition, the third column shows the significance of the variables of gas path temperature and coupon angle in terms of a P-value. Values less than 0.05 are considered significant for the MLR model.

$$(1-1) \quad \sqrt{D_{T,\theta}} = \beta_0 + \beta_T * T + \beta_\theta * \theta + \varepsilon$$

Table 1-5: Multiple linear regression (MLR) model parameters using test data input into JMP®.

Parameter	Value	Prob > t
β_0	-60.25708	<.0001*
β_T	0.0613822	<.0001*
β_θ	0.046278	0.0105

When making a prediction, the estimated values produced from the MLR model will be used in place of the parameters. For example, to estimate the sand deposited per area at 1025 °C and 45° coupon angle, use Equation (1-2). The random error term is disregarded for the calculation since it cannot be quantified.

$$(1-2) \quad \sqrt{D_{1025^{\circ}\text{C},45^{\circ}}} = \beta_0 + \beta_T * (1025) + \beta_{\theta} * (45)$$

Overall, the model's adjusted R-Squared value of 0.6493 explains the proportion of information of the response (average deposition) that the model is able to determine. Therefore, the MLR model can explain 64.93% of the average deposited particles per area from coupon angle and average gas path injection temperature. The remaining 35.07% may be the result of random error such as environmental testing conditions sand injection rates, etc. For instance, if more control variables are added to the testing matrix such as sand injection rate, the adjusted R-Squared value may increase. However, the additional variables may confound with other existing variables that are already being tested and may not improve the adjusted R-Squared value significantly.

1.7. Conclusions

Deposition increases with increasing gas path temperatures and coupon angle. From prior studies, deposition is dependent on substrate temperature and particulate type [15]. In this study, the coupon surface temperatures is a function of gas path temperature. Based on testing conditions, the substrate surface temperature is lower than the actual gas path temperature due to thermal losses inside the test section. Despite the lower coupon surface temperature, the onset of deposition did occur below the sintering temperature of the ATD [22].

The statistical model developed for this study is intended to quantify deposition with some uncertainty based on gas path temperature and coupon angle. Other factors, such as coupon surface temperature, are not directly considered due to testing limitations. An MLR model is able to estimate average deposition of particles per area as a function of gas path temperature and coupon angle. The strength of this model indicates that about 65% of the deposition can be explained by gas path temperature and coupon angle. Therefore, improvement in the statistical model is necessary to explain the remaining model uncertainty. Surface temperature and ATD injection rates may explain most of the remaining variation.

The methodology described in this study provides significant flexibility for estimating deposition with two or more testing variables. The basic model can be expanded to complex functions to account for other variations and provide a basis for estimating all conditions where deposition may occur in hot engine environments.

1.8. Acknowledgments

The work presented here was supported by Rolls-Royce Plc., especially Brett Barker, Dr. Kwen Hsu, and Paul Davis.

1.9. References

- [1] Reagle, C. J., Delimont, J. M., Ng, W. F., Ekkad, S. V., and Rajendran, V. P., 2013, “Measuring the coefficient of restitution of high speed microparticle impacts using a PTV and CFD hybrid technique,” *Meas. Sci. Technol.*, 24(10), p. 105303.
- [2] Delimont, J. M., Murdock, M. K., Ng, W. F., and Ekkad, S. V., 2014, “Effect of Near Melting Temperatures on Microparticle Sand Rebound Characteristics at Constant Impact Velocity,” *ASME Turbo Expo 2014, Volume 1A: Aircraft Engine; Fans and Blowers*, ASME, Dusseldorf, pp. 1–11.
- [3] Delimont, J. M., Murdock, M. K., Ng, W. F., and Ekkad, S. V., 2014, “Effect of Temperature on Microparticle Rebound Characteristics at Constant Impact Velocity,” *ASME Turbo Expo 2014*, pp. 1–11.
- [4] Reagle, C. J., Delimont, J. M., Ng, W. F., and Ekkad, S. V., 2014, “Study of Microparticle Rebound Characteristics Under High Temperature Conditions,” *J. Eng. Gas Turbines Power*, 136(1), p. 011501.
- [5] Singh, S., Tafti, D. K., Reagle, C. J., Delimont, J. M., Ng, W. F., and Ekkad, S. V., 2014, “Sand transport in a two pass internal cooling duct with rib turbulators,” *Int. J. Heat Fluid Flow*, 46, pp. 158–167.
- [6] Delimont, J. M., Murdock, M. K., Ng, W. F., and Ekkad, S. V., 2015, “Effect of Temperature on Microparticle Rebound Characteristics at Constant Impact Velocity—Part II,” *J. Eng. Gas Turbines Power*, 137(11), p. 112604.

- [7] Delimont, J. M., Murdock, M. K., Ng, W. F., and Ekkad, S. V., 2015, “Effect of Temperature on Microparticle Rebound Characteristics at Constant Impact Velocity—Part I,” *J. Eng. Gas Turbines Power*, 137(11), p. 112603.
- [8] Gabbard, C. B., LeLevier, R. E., and Parry, J. F. W., 1982, *Dust-Cloud Effects on Aircraft Engines - Emerging Issues and New Damage Mechanisms (U)*, Marina del Rey.
- [9] Hinton, H. L. J., Warren, D. R., and Schulz, T. J., 2001, *Operation Desert Storm: Bradley Fighting Vehicle, Abrams Tank, Apache Helicopter, Patriot Missile System and Foreign Government and Individual Contributions*, DIANE Publishing.
- [10] Whittle, R., 2015, “Fatal Crash Prompts Marines to Change Osprey Flight Rules,” *Break. Def.*
- [11] Dunn, M. G., Padova, C., Moller, J. E., and Adams, R. M., 1987, “Performance Deterioration of a Turbofan and a Turbojet Engine Upon Exposure to a Dust Environment,” *J. Eng. Gas Turbines Power*, 109(3), p. 336.
- [12] Batcho, P. F., Moller, J. C., Padova, C., and Dunn, M. G., 1987, “Interpretation of Gas Turbine Response Due to Dust Ingestion,” *J. Eng. Gas Turbines Power*, 109(3), p. 344.
- [13] Dunn, M. G., Padova, C., and Adams, M. R., 1987, “Operation of Gas Turbine Engines in Dust-Laden Environments,” p. 16.
- [14] Dunn, M. G., 1991, *Exposure of Air Breathing Engines to Nuclear Dust Environment (U)*, Buffalo.
- [15] Kim, J., Dunn, M. G., and Baran, A. J., 1996, *The “Most Probable” Dust Blend and Its Response in the F-100 Hot Section Test System (HSTS)*, Buffalo; Alexandria.
- [16] Weaver, M., Dunn, M. G., and Heffernan, T., 1996, “Experimental Determination of the Influence of Foreign Particle Ingestion on the Behavior of Hot-Section Components Including Lamilloy,” *ASME Turbo Expo 1996*, ASME, Birmingham, pp. 911–917.
- [17] Cowherd, C., 2007, *Sandblaster 2 Support of See-Through Technologies for Particulate Brownout Task 5 Final Technical Report*.
- [18] Smialek, J. L., Archer, F. a., and Garlick, R. G., 1991, *The Chemistry of Saudi Arabian Sand - A Deposition Problem on Helicopter Turbine Airfoils*.
- [19] Smialek, J. L., Archer, F. a., and Garlick, R. G., 1994, “Turbine Airfoil Degredation in the Persian Gulf War,” *J. Met.*, 46(12), pp. 39–41.

- [20] Hamed, A., Tabakoff, W. C., and Wenglarz, R. A., 2006, "Erosion and Deposition in Turbomachinery," *J. Propuls. Power*, 22(2), pp. 350–360.
- [21] Song, W., Hess, K. U., Damby, D. E., Wadsworth, F. B., Lavallée, Y., Cimarelli, C., and Dingwell, D. B., 2014, "Fusion characteristics of volcanic ash relevant to aviation hazards," *Geophys. Res. Lett.*, 41(7), pp. 2326–2333.
- [22] Kueppers, U., Cimarelli, C., Hess, K.-U., Taddeucci, J., Wadsworth, F. B., and Dingwell, D. B., 2014, "The thermal stability of Eyjafjallajökull ash versus turbine ingestion test sands," *J. Appl. Volcanol.*, 3(1), p. 4.
- [23] Turner, E. R., Wilson, W. D., Hylton, L. D., Kaufman, R. M., 1985, *Turbine Vane External Heat Transfer, Volume 1. Analytical and Experimental Evaluation of Surface Heat Transfer Distributions with Leading Edge Showerhead Film Cooling*, Indianapolis.
- [24] Hylton, L. D., Nirmalan, V., Sultanian, B. K., and Kaufman, R. M., 1988, *The Effects of Leading Edge and Downstream Turbine Vane Heat Transfer*, Indianapolis.
- [25] Nealy, D. A., Mihelc, M. S., Hylton, L. D., and Gladden, H. J., 1983, "Measurements of heat transfer distribution over the surfaces of highly loaded turbine nozzle guide vanes," *J. Eng. Gas Turbines Power*, 106(January 1984), pp. 149–158.
- [26] Hylton, L. D., Mihelc, M. S., Turner, E. R., Nealy, D. a., and York, R. E., 1983, *Analytical and Experimental Evaluation of the Heat Transfer Distribution over the Surfaces of Turbine Vanes*, Indianapolis.
- [27] Livingood, J. N. B., and Hrycak, P., 1973, *Impingement heat transfer from turbulent air jets to flat plates: A literature survey*, Washington, D.C., USA.
- [28] Wu, C. F. J., and Hamada, M. S., 2009, *Experiments: Planning, Analysis, and Optimization*, Wiley.
- [29] Norton, B. J., and Strube, M. J., 1986, "Guide for the interpretation of two-way analysis of variance," *Am. Phys. Ther. Assoc.*, 66(3), pp. 402–12.
- [30] Oehlert, G. W., 2010, *A First Course in Design and Analysis of Experiments*.
- [31] Jarvis, E. A. A., and Carter, E. A., 2003, "Exploiting covalency to enhance metal-oxide and oxide-oxide adhesion at heterogeneous interfaces," *J. Am. Ceram. Soc.*, 86(3), pp. 373–386.

2. Paper #2: Experimental Investigation of the Onset of Sand Deposits on Hastelloy-X between 1000 °C and 1100 °C

2.1. Abstract

Deposit formation on turbine hardware in propulsion turbine engines can occur in many arid regions globally. Characterizing crystalline deposits on metallic substrates can aid in component resilience and health monitor algorithms during particle ingestion. This study has developed two statistical models for prediction from acquired experimental data for the onset of deposits. The prediction models are for crystalline particulate (Arizona Road Dust) deposits on a flat rectangular Hastelloy-X test coupon. Particle impingement angles varied between 20° and 80° in experimental flow temperatures of 1000 °C to 1100 °C. Averaged deposits are methodically quantified through normalized particle deposit tallies per area and percent coverage of the surface using microscopic imaging and image processing programs. Deposit accumulation is a quadratic function of both near-surface coupon temperature and coupon angle.

2.2. Nomenclature

ARD	Arizona Road Dust
CCD	Central Composite Design
NASA	National Aeronautical and Space Administration (United States of America)
NGV	Nozzle Guide Vane
PPMW	Parts Per Million by Weight
RMS	Root Mean Square
VTAR	Virginia Tech Aerothermal Rig

2.2.1. Symbols

D_P	Average particle deposits per area
D_{CA}	Average percent coverage area
T_{NS}	Near-surface coupon temperature
θ	Coupon angle (degrees)

2.3. Introduction

Propulsion turbine engine particulate ingestion is a common issue in many arid regions. Typically, sand and dust ingested can produce glassy deposits on combustor and turbine components, which can cause detrimental effects ranging from reduced performance to complete engine failure. Characterizing deposits depends on a variety of conditions, such as the mass ingested, particulate constituents, turbine component materials, and operating conditions. There are a variety of methods to combat detrimental effects including reducing engine power during an ingestion event or increase the service intervals for the exposed turbine engines. However, during extreme dust ingestion conditions, catastrophic engine failure is possible. This study provides results from analysis of data from a conducted experiment involving the initial deposits of crystalline particulate, Arizona Road Dust (ARD), on a flat rectangular Hastelloy-X test coupon as a relative analogue to actual turbine components. The data from the experiment is aggregated and analysed through two statistical models for prediction.

Prominent examples of partial and complete turbine engine failure in airframes and equipment have been documented for several decades. For instance, during the Mount St. Helens eruption, an L-100 aircraft had two engines fail while the other two had partial power loss while flying below the ash cloud after the eruption began [1]. Recently, on May 17, 2015, a United States Marine MV-22 Osprey had a fatal crashed during a training exercise in dusty conditions while performing a hover manoeuvre. The right engine flamed out causing the craft to drop 26 meters to the ground. Two US Marines were killed in the event with the remaining crew sustaining mild to severe injuries [2]. The post-accident report cited glassy deposits on the turbine section components as one of the direct causes of the engine failure.

Ingested particulate can be separated into two general categories, crystalline and amorphous. Crystalline particles, henceforth referred to as sand, are commonly found in desert regions whereas amorphous particles are found in volcanic ash. Since sand can vary in composition and size, previous airframe testing determined the quantity and sizing of lofted sand in brownout conditions [3]. Typical lofted sand concentrations in extreme rotor wash conditions (depending on airframe) can be as high as 5000 parts per million by weight (PPMW). In addition, sand composition can vary depending on geographic location. For instance, even in a relatively small region in the Dhahran area the composition of sand is primarily SiO_2 and Al_2O_3 but can vary in

large proportions [4, 5]. The large variation in sand composition will affect the deposit formation and accumulation [6].

Crystalline material phase structure and motion mechanisms relative to temperature can determine the probability that a particle will stick to a substrate. Since sand is composed of a variety of base constituents, the response of each non-homogenous material can vary at high temperatures. Generally, particulate material proceeds through four structure phases as temperature increases through the sintering process. They are designated as shrinking, deformation, hemisphere, and flow phases [7]. Each phase temperature can vary depending on the particulate constituents. In the context of turbine engine deposits, as the combustion temperatures increase the particulate effectively softens or liquefies, which increases the probability of deposits onto a turbine component substrate. Particulate motion mechanisms associated with deposition are inertial impaction, turbulent diffusion/eddy impaction, Brownian diffusion, and thermophoresis [8]. Previous testing and modelling has demonstrated deposits as a function of particulate sizing. Stokes number is usually able to characterize the likelihood of a particle trajectory before impacting a substrate using the particle size. For Stokes numbers greater than unity, which are typically larger than one micron, the particulate is more likely to be dominated by inertial effects and resist changing direction due to the flow field. Since this study utilizes 20 to 40 μm ARD, the primary mechanism is inertial impaction for all test conditions.

2.4. Experiment Method

All test were performed using the Virginia Tech Aerothermal Rig (VTAR) at the Advanced Propulsion and Power Laboratory at Virginia Tech. VTAR is capable of an 1100 °C maximum flow temperature at the test section for various sand injection concentrations. Tests were conducted at flow temperatures between 1000 °C and 1100 °C with coupon angles of 20°, 50°, and 80°. The experimental design is a Central Composite Design (CCD) with repeated central tests. Quantified deposit data uses a multiple linear regression as a function of near-surface coupon temperature and coupon angle.

2.4.1. Virginia Tech Aerothermal Rig

VTAR was donated by Rolls Royce (Indianapolis, IN) to Virginia Tech in 2010. The previous application prior to the donation was heat transfer studies of cascade turbine airfoils [9-12]. The test equipment was repurposed for high temperature particle tracking studies by quantifying the coefficient of restitution [13,14]. The most recent study was for ARD deposit accumulation for very high sand loading and concentrations [15].

Figure 2-1 is a rendering of VTAR's current configuration for sand deposition testing. Propane is the fuel source for the sudden expansion burner. The total flow rate leaving the burner is about 0.06 kg/s depending on the flow temperature. The equilibration tube is constructed of SS 310 with an inner diameter of 7.62 cm. The distance from the sand injector point to the end of the equilibration tube inside the test section is about 2.22 m. The equilibration tube length allows a sufficient amount of time for the temperature of the sand particles to equalize with the flow temperature. The injector inside the equilibration tube is directed upstream to promote sufficient mixing. A constant flow velocity leaving the equilibration tube is 70 ± 2 m/s for all tests in this study to maintain consistency from the previous studies using VTAR [13-15]. The maximum flow temperature that can be achieved at the coupon is 1100 °C.

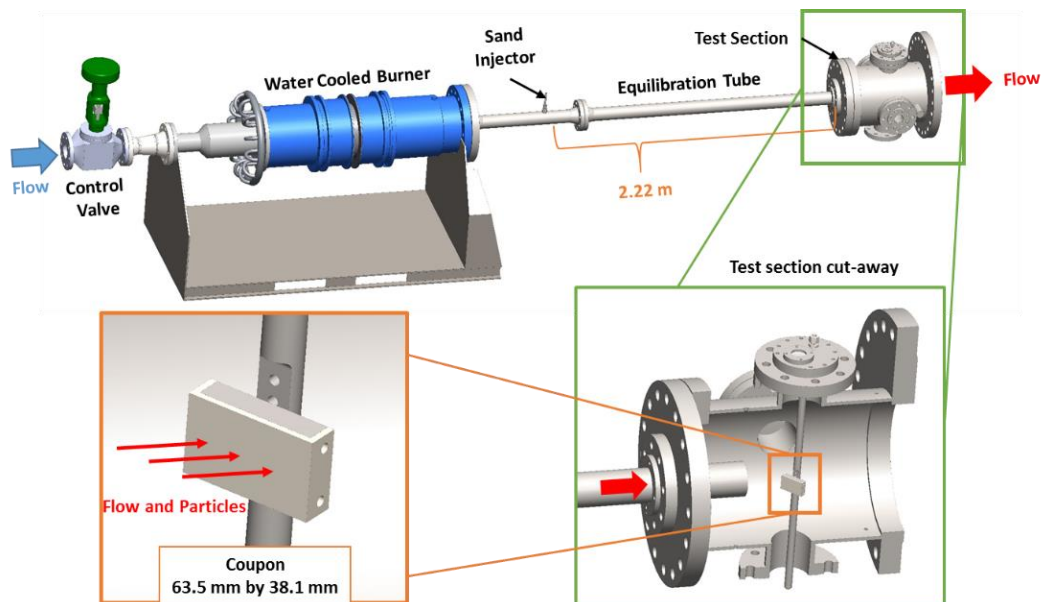


Figure 2-1: The Virginia Tech Aerothermal Rig (VTAR) utilized for deposition testing between 1000 °C and 1100 °C, highlighting the test section cut-away view and the associated coupon.

The test sand is dried in an oven at 120 °C for a minimum of 12 hours prior to a test. Most excess water trapped in the particulate evaporates, which prevents “clumping” during the injection process. Dry ARD is entrained in a flow separate from the main flow using a conveyor-venturi injection system. Sand is placed on a conveyor belt inside a sealed box to prevent contamination from environmental dust and humidity levels. The conveyor belt moves and drops the sand into venturi vacuum pump. A conveyor scraper is used to passively ensure a majority of the sand drops into the pump. From system testing, mass losses are less than 0.01 grams from the conveyor into the vacuum venturi pump. To equalize the pressure inside the box due to the venturi vacuum pump, a particulate filter and an air drying system ensures that the local environmental humidity does not alter the sand consistency during testing. Secondary containment around the conveyor belt reduces potential agitation of the sand due to air movement in the primary containment box. After the sand moves through the venturi vacuum pump, the sand laden flow travels through a hose that is attached to the injector nozzle on the equilibration tube.

The coupon angle illustrated in Figure 2-2 (LEFT), is the acute angle between the flow and the surface of the coupon where 0° is parallel and 90° is perpendicular to the flow. The coupon can be rotated in 10° increments along the vertical axis of the test section. Flow temperature is measured with three K-type thermocouples placed along the horizontal midline next to the coupon leading edge as well as above and below the coupon while being centered horizontally, illustrated in Figure 2-2 (RIGHT). Due to the size and angle of the coupon relative to the equilibration tube, all the thermocouples are within the gas path. Two K-type thermocouples are placed directly behind the coupon to measure near-surface coupon temperature. The distance from the end of the equilibration tube to the leading edge of the coupon is approximately 10 cm. The distance decreases by about 2 to 3 cm during operations due to the thermal expansion of the tube into the test section via a slip joint. Hastelloy-X is the coupon material, which is the same from previous studies [13-15].

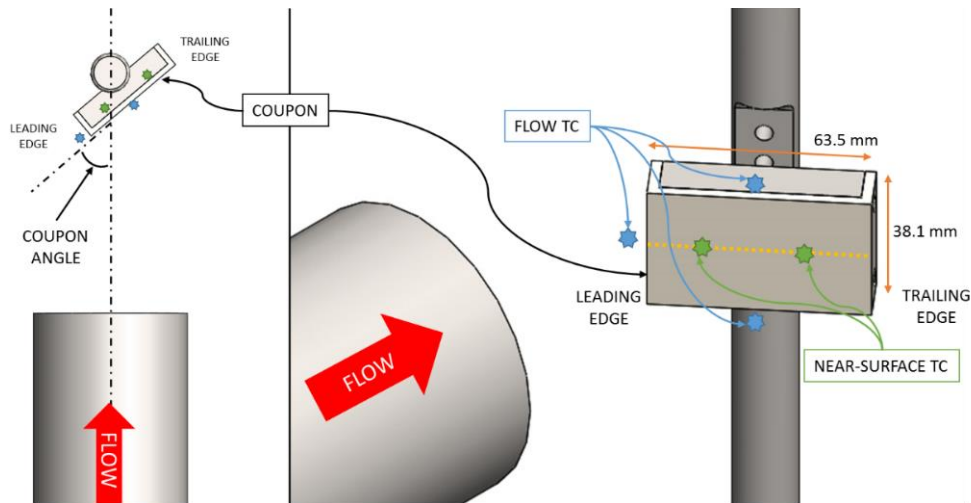


Figure 2-2: Two views of the coupon arrangement. (LEFT) Top-down view of coupon and equilibration tube with the test section casing and flanges hidden. (RIGHT) An isometric view of the coupon and equilibration tube indicating thermocouple placement top and bottom of the coupon. The yellow dashed line across the coupon surface indicates the horizontal midline of the coupon and gas flow path.

2.5. Experiment Testing Conditions

Controlled factors for this study are bulk flow temperature and coupon angle. Deposited particles per area and percent coverage on the coupon surface by the deposits are the dependent variables. Table 2-1 provides a summary of the experiment test conditions. Flow temperature during injection is maintained within 5 °C of the goal temperature, either 1000 °C, 1050 °C, or 1100 °C. Near-surface coupon temperatures are measured for the subsequent statistical model, see Figure 2-2. The near-surface and surface temperatures of the coupon vary depending on the coupon angle (20°, 50°, or 80°) due to various heat transfer mechanisms during testing inside the test section. Only 10 ± 0.005 grams of ARD are used per test. The coupon is composed of Hastelloy-X and is polished to a mirror-like finish before each test with a measured root mean square roughness of less than 0.2 μm to ensure surface roughness effects are minimized for deposition.

Table 2-1: Constant test conditions for varying flow temperature and coupon angle testing.

Bulk Flow Velocity	70 ± 2 m/s
Desired Gas Path Temperature Range	1000 °C, 1050 °C, and 1100 °C
Particulate Type/Size	ARD, 20 – 40 µm
Injection Rate	0.0570 to 0.0646 g/s
Total Sand Loading	10 ±0.005 grams
Coupon Angles	20°, 50°, and 80°
Coupon Material	Hastelloy-X
Coupon Surface Roughness	≤ 0.2 µm RMS
Coupon Thickness	3.175 mm
Particle Stokes Number	~1.6 (20 µm) to 6.8 (40 µm)

The 20 to 40 µm ARD batch used in all tests is ISO test dust grade from Powder Technologies Inc. The Stokes number for the experiment is between 1.6 and 6.8 depending on local velocity near the coupon surface. The mean diameter of the ARD is 26.58 µm with a median diameter of 27.3 µm. About 90% of the sand volume is between 20 and 40 µm, with the remaining 10% being less than 20 µm. Silicon and aluminum oxides are the primary constituents of ARD. An earlier study determined that ARD has a sintering temperature (shrinking phase) of 1100°C for sizing less than 63 µm. Since the ARD is in a softened state, the sand particles may adhere to the Hastelloy-X surface [16]. The authors are aware that ARD is not an accurate analogue of airborne sands and dusts found across the world [17]. In addition, the particles typically entering the hot-section of a turbine engine have a mean diameter less than 10 µm [18]. However, the ARD sizing used for this study improves the detection of deposited particles for post-test image processing and analysis as well as allows a comparison to previous and potentially future deposition studies at Virginia Tech [13-15].

VTAR’s sand injection system has been updated from the previous microparticle rebound and deposition studies [13-15] to allow for precise injection rate control that would be similar to turbine engine dust ingestion conditions. Dust concentrations ingested by turbine engines can be as high as 5,000 PPMW for extreme low visibility conditions [3]. Injection rates for this study are 0.0570 to 0.0646 g/s, equivalent to 800 to 1000 PPMW, for approximately three minutes. Sand concentration variation is directly correlated to the variation in mass flow rate per test through the

burner. Based on the operational parameters of VTAR, to maintain the velocity at 70 m/s as temperature increases, the mass flow rate must decrease. Regardless of the mass flow rate of the gas path and the associated concentration, the equilibration tube allows the particles to attain thermal and momentum equilibrium with the main flow before impacting or being diverted around the coupon.

For each test, VTAR is brought up to steady-state flow conditions at the appropriate flow temperature and velocity. Flow temperature is set by the maximum temperature associated with each test angle (Figure 2-2). For instance, at angles of 20° and 50°, the maximum temperature is the leading edge temperature. However at 80°, the maximum temperatures are on the top and bottom of the coupon. Since the flow is being deflected around the coupon there are recirculation zones on the trailing and leading edges, which lowers the measured temperature at those locations. Due to the variation in flow temperature measurement locations and heat transfer mechanisms inside the test section, the primary variable compared to deposits is the average near-surface coupon temperature (Figure 2-2). Experimental relationships for jet impingement onto a flat plate [19] determined the heat transfer coefficients to estimate coupon surface temperatures for each test angle. Using the heat transfer coefficient and estimating the radiative heat transfer, the variation of temperature between the surface and near-surface is less than 5 °C depending on coupon angle for the experimental setup. Therefore, near-surface temperature is used as an independent variable for the statistical modelling.

ARD deposit accumulation on the inner walls of the equilibration tube is negligible for all testing. Periodic borescope inspections of the equilibration tube indicate minimal deposit accumulation. Regardless, molten sand particles may adhere to the inside of the stainless steel equilibration tube during testing. However, during the cool-down process after each test, any deposited material most likely delaminated from the equilibration tube and carried downstream. Since the equilibration tube has minimal deposits between tests, one test result should not affect a subsequent tests. Future studies will be necessary to accurately quantify any deposits that may occur on parallel flow surfaces using ARD.

2.5.1. Statistical Modelling Method

A multiple linear regression model is developed for estimating initial ARD deposits at various coupon angles and near-surface temperatures. There are a total of nine possible test combinations for flow temperature and angle. Primary control factors are the flow temperatures set at 1000 °C, 1050 °C and 1100 °C and three coupon angles set at 20°, 50°, and 80°. A Central Composite Design (CCD) is the most popularly used experimental design for fitting a second-order response surface [20]. A CCD is composed of factorial points for all possible high and low combinations of the factors, center points which provide information about curvature of the response surface, and axial points which allow for estimation of quadratic effects. Since there are two factors with three levels each, a cuboidal CCD assists with studying curvature effects of the responses. With a minimum of nine possible combinations, three additional tests are performed at the centre levels for coupon angle (50°) and flow temperature (1050 °C) to ensure repeatability and curvature effects. By comparison, the CCD in this study uses 12 total tests, while a full factorial design with test triplication would require a minimum of 27 tests. The results from the CCD can be used for efficient estimation of first and second-order terms of the response surface of interest.

The fully randomized test order for the CCD is generated by JMP[®]. Randomizing the order of the experimental trials reduces bias caused by nuisance factors, such as equipment warm-up effects and daily atmospheric conditions. Each ARD sample is also randomly assigned to each experimental test condition.

2.6. Results and Analysis

Deposits are quantified through microscopic images and processed to identify the normalized particle deposit tallies per square millimeter and percent coverage of the Hastelloy-X coupon surface. Deposits from both metrics are identified automatically and manually validated for each acquired image. The deposit data is averaged per test and combined to create two statistical prediction models. Heavy particle overlapping is observed for flow temperatures above 1050 °C and 50° coupon angle.

2.6.1. Data Acquisition and Reduction

Figure 2-3 (LEFT) is a comparison example of the coupon surface at 20x magnification before and after each test at 1050 °C at 50°. Each microscopic image is the about 698 μm by 522 μm . Deposits metrics are average particles per area (particles per square millimeter) and average percent coverage. Quantifying the total deposits on the coupon surface uses a similar to the earlier deposition study at Virginia Tech [15].

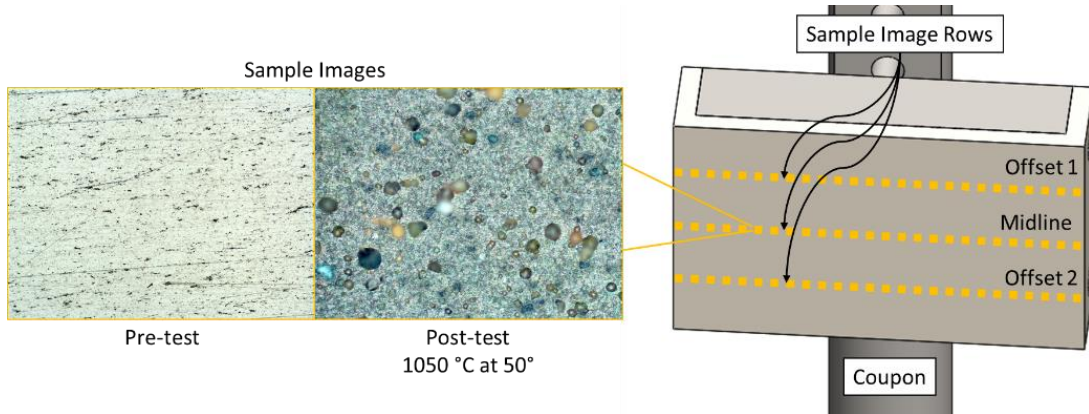


Figure 2-3: (LEFT) Pre-test and post-test surface sample image comparison showing the deposits and Hastelloy-X surface. The image size is 698 μm by 522 μm at 20x magnification. (RIGHT) Rendered image of the coupon surface that highlights the locations of the sample image rows that are located at the midline, and the quarter and three quarter locations vertically along the horizontal axis.

The microscope system available requires manual acquisition of each location on the coupon. Based on the coupon orientation in the test section, three series of images are acquired across the horizontal axis of the coupon. Figure 2-3 (RIGHT) shows the location of each image series, which are at one quarter, one half, and three quarters the relative vertical distance of the coupon. Three sample image rows provide triplicate data sets for each test condition and validates the coupon exposure to the main gas path flow conditions. From each sample image row, approximately 50 to 60 images are acquired in relatively equal spacing for each cord across the surface from the leading edge towards the trailing edge. An exact location cannot be determined with manual acquisition so equal spacing is assumed for all images across each series.

Each image is acquired with the focus set to the Hastelloy-X substrate, which causes the particle deposits to be slightly out of the focus plane resulting in a distinct boundary between the

deposit and the heterogeneous surface pattern. Using the pattern and texture differences from the Hastelloy-X surface and deposits on the coupon surface, each image is processed using several functions from the MATLAB[®] Visual Processing Toolbox. The image processing script is able to automatically identify most deposit particles and regions larger than 10 μm across for each image. Particle deposits less than 10 μm in diameter are disregarded based on the size distribution of the ARD supplied for this study. After the automatic selection process, each image is manually checked for incorrect identification and corrected if necessary. The combination of automatic and manual identification is capable of low variability and high repeatability between analysts.

Delamination of the particles from the coupon after testing (during VTAR cool-down) and during image processing is not observed. The local bond between Hastelloy-X and SiO_2 , a primary constituent of ARD, is a strong atomic level bond that resists thermal cycles. Prior research has implied that a crystalline SiO_2 layer between a nickel-based alloy and a crystalline thermal barrier coating would provide the bond strength necessary to prevent delamination during thermal cycling [21].

2.6.2. Raw Data

Table 2-2 is the testing order, near-surface temperatures, and average deposit data for each test condition for all three sample image rows. As expected, deposits typically increase with increasing surface temperature and coupon angle.

Table 2-2: Aggregated deposit data for each test as well as the average near-surface temperature.

Test Order	Flow Temperature (°C)	Coupon Angle (°)	Average Near-Surface Temperature (°C)	Average Particles per mm ²	Average Percent Coverage
1	1000	50	879.10	13	0.806
2	1050	50	916.69	210	7.444
3	1100	50	965.52	364	24.509
4	1100	20	950.84	139	6.631
5	1050	50	917.28	167	6.269
6	1050	80	897.51	193	8.476
7	1000	80	867.00	37	1.431
8	1100	80	933.56	335	21.871
9	1050	50	916.54	172	6.614
10	1050	50	915.81	155	6.843
11	1000	20	876.66	6	0.342
12	1050	20	910.75	49	2.196

Figure 2-4, correlates the deposit data with near-surface temperature shows that the deposit trends increase with coupon angle. The repeated tests at 1050 °C and 50° coupon angle show very little variation between the four tests for both deposits per square millimeter and percent coverage area. Comparing the raw deposit data for particle deposits per square millimeter and percent coverage area, the maximum total deposits observed occurs at 1050 °C flow temperature at 80° coupon angle. Near-surface temperatures at 80° coupon angle are lower than their counterparts at 20° and 50°. Convective recirculation area behind the coupon and radiative heat transfer mechanisms result in lower observed substrate temperatures. Specifically, at 80° coupon angle, there is a large stagnation region that develops in front of the coupon. The stagnation region can cause a large portions of the particles to be diverted around the coupon or decrease in velocity where they will not deposit. Reduced deposits at high angles and high temperatures has been observed before for a previous study at Virginia Tech that evaluated deposits under very high particulate loading at 1100 °C and 90° coupon angle [15].

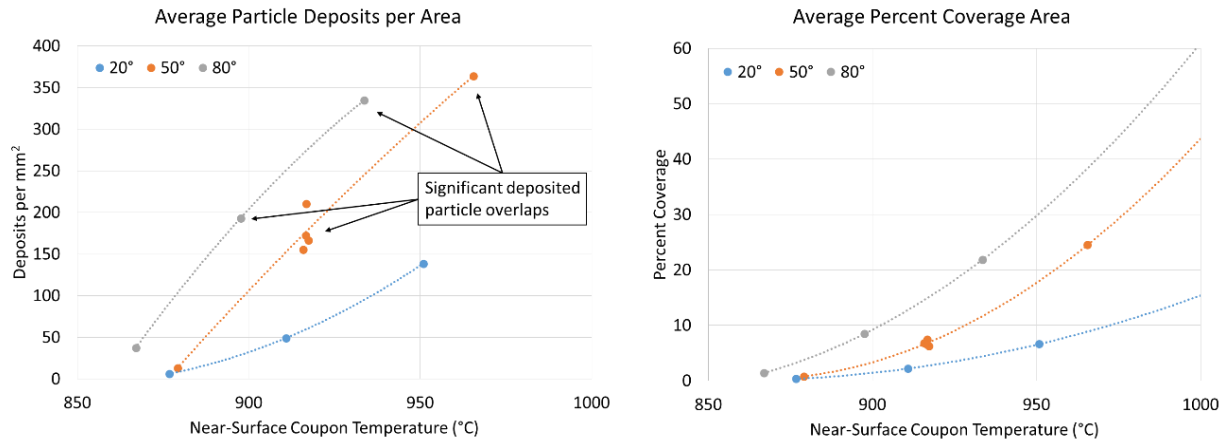


Figure 2-4: (LEFT) Average particle deposits per square millimeter on the coupon and (RIGHT) average deposit percent coverage area on the coupon. Both responses are plotted against near-surface coupon temperature. The average deposits per square millimeter is less than anticipated due to significant deposited particles overlapping on the surface.

Despite the underestimated particle deposits per area, a deposit per area estimated range is calculated using the percent coverage area data, Figure 2-5. Average deposits per square millimeter increase linearly while the percent coverage area increases at a quadratic rate. Deposits greater than 1050 °C flow temperatures and at 50° coupon angles show significant particle overlaps and large deposit regions. Overlapping particles are relatively indistinguishable for the image processing scripts and manual validation, which implies particle counts per image are underestimated at higher surface temperatures and coupon angles. Assuming the maximum and minimum size of a potential particle deposit has a diameter between 20 μm and 40 μm , the lower and upper bounds are calculated. Particle deposits per square millimeter is within the estimate boundaries but the raw data rate of increase does not correlate to the estimated boundary rates. For this study, both average particle deposit and percent coverage area data indicate the necessity to use a combination of prediction models for the onset of deposits.

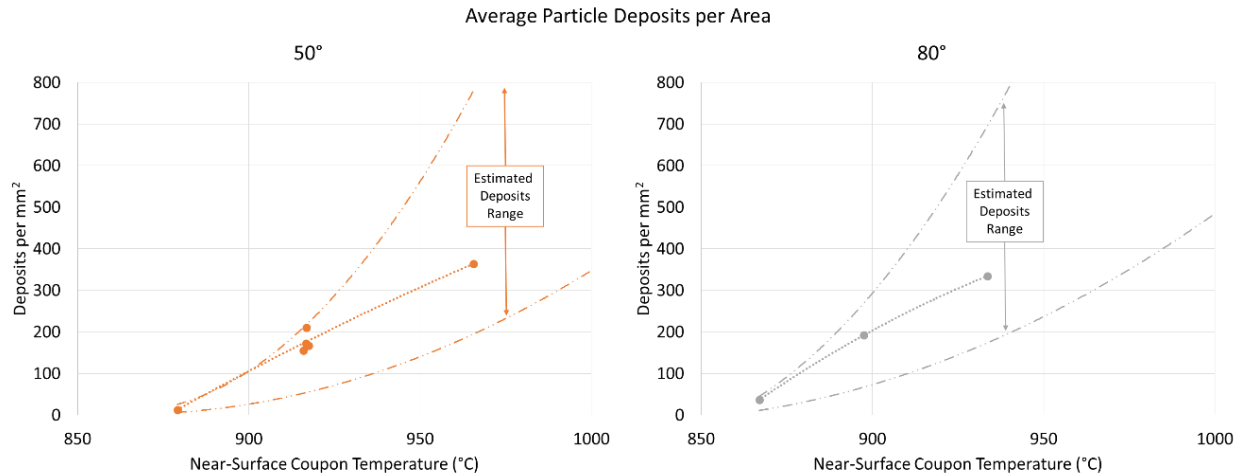


Figure 2-5: Particle deposits per area for the 50° and 80° coupon angle test cases with an estimated interval using the coverage area data.

2.6.3. Statistical Models for Prediction

Average deposits per area and percent coverage area are the primary dependent variables for both statistical models for prediction. The near-surface temperature and coupon angle are the predictors for the dependent variables of average deposits per area and percent coverage. Near-surface temperature is converted from Celsius to Kelvin, for an absolute temperature scale. JMP® and MATLAB® statistical modelling results are compared and validated for the prediction models. All predictors included in the prediction models presented are statistically significant at the 0.05 level of significance. This implies that predictors in the final models are useful in predicting average deposits per area and percent coverage.

The average particle deposits per square millimeter predictor model (Equation (2-1)) has a strong correlation with both near-surface temperature and coupon angle predictors. The R^2 and adjusted R^2 values are greater than 90% (Table 2-3). The model contains an interaction between near-surface temperature and coupon angle. This means that the effect of near-surface temperature on the average particle deposits per square millimeter depends on the coupon angle.

$$(2-1) \quad D_p = -4179.2 + 3.5266 T_{NS} + 3.132 \theta + 0.045799 (T_{NS} - 1185.4)(\theta - 50)$$

The average deposit percent coverage prediction model (Equation (2-2)) has a stronger correlation for the near-surface temperature and coupon angle predictors compared to the

Equation (2-1) model. The percent coverage model uses second-order predictors for near-surface temperature and coupon angle. Second-order predictors are necessary to achieve high the R^2 and adjusted R^2 values shown in Table 2-3. A quadratic response correlates with the average percent coverage trends in Figure 2-4. By comparison, the deposits per area data in Figure 2-4 are relatively linear for the 50° and 80° cases, which will overpower the quadratic response of the 20° tests. As mentioned in previously in Section 2.6.2 there is significant deposit overlapping for the higher coupon angles and temperatures, that results in underestimation. Therefore, the percent coverage area prediction model is more representative of deposits compared to the deposits per area model at higher temperatures.

$$\begin{aligned}
 D_{CA} = & -269.63 + 0.22378 T_{NS} + 0.20534 \theta \\
 & + 0.004718 (T_{NS} - 1185.4)(\theta \\
 & - 50)0.0021594 (T_{NS} - 1185.4)^2 \\
 & + 0.0014217 (\theta - 50)^2
 \end{aligned}
 \tag{2-2}$$

Table 2-3: R-squared and adjusted R-squared values for particle deposits per area (Equation 2-1) and deposit percent coverage (Equation 2-2).

	Particle Deposits per Area	Deposit Percent Coverage
R-squared	0.973	0.994
Adjusted R-squared	0.963	0.989

2.7. Conclusion

This study developed two statistical prediction models with experimental data for the onset of ARD sand deposits on a flat Hastelloy-X coupon at high temperatures as quadratic functions of near-surface coupon temperature and coupon angle. Flow temperatures are between 1000 °C and 1100 °C at 70 m/s and an ARD concentration is between 800 to 1000 PPMW with coupon angles are 20°, 50°, and 80°. Deposit accumulation between 1050 °C and 1100 °C flow temperatures for coupon angles greater than 50° has significant particle deposit overlapping. High levels of particle deposit overlap result in an underestimating prediction model (Equation (2-1)) above about 1050 °C. An average percent coverage area prediction model (Equation (2-2)) is able to quantify deposit accumulation despite the high levels of particle overlap. Therefore, a combination of Equation (2-1) and Equation (2-2) is necessary to estimate surface deposits. In addition, particle

deposit overlap and high substrate percent coverage indicates a shift towards utilizing alternative data processing and prediction models. Using mass or surface roughness analysis of a test specimen is a subsequent data acquisition method that has been used in other studies to establish a way of estimating deposit accumulation.

This experiment can be expanded for future test scenarios. For instance, future experiments may involve particle tracking to characterize deposits as a function of near-surface temperature and particle impact vectors. In addition, altering coupon temperature as an analogue to turbine cooled hardware can expand the current statistical model.

2.8. Acknowledgments

The work presented here was supported by Rolls-Royce Plc., especially Brett Barker, Dr. Kwen Hsu, and Paul Davis as well as Virginia Tech's Laboratory for Interdisciplinary Statistical Analysis (LISA).

2.9. References

- [1] Gabbard, C. B., LeLevier, R. E., and Parry, J. F. W., 1982, Dust-Cloud Effects on Aircraft Engines - Emerging Issues and New Damage Mechanisms (U), Marina del Rey.
- [2] Whittle, R., 2015, "Fatal Crash Prompts Marines to Change Osprey Flight Rules," Break. Def.
- [3] Cowherd, C., 2007, Sandblaster 2 Support of See-Through Technologies for Particulate Brownout Task 5 Final Technical Report.
- [4] Smialek, J. L., Archer, F. a., and Garlick, R. G., 1991, The Chemistry of Saudi Arabian Sand - A Deposition Problem on Helicopter Turbine Airfoils.
- [5] Smialek, J. L., Archer, F. a., and Garlick, R. G., 1994, "Turbine Airfoil Degredation in the Persian Gulf War," J. Met., 46(12), pp. 39–41.
- [6] Kim, J., Dunn, M. G., and Baran, A. J., 1996, The "Most Probable" Dust Blend and Its Response in the F-100 Hot Section Test System (HSTS), Buffalo; Alexandria.
- [7] Song, W., Hess, K. U., Damby, D. E., Wadsworth, F. B., Lavallée, Y., Cimorelli, C., and Dingwell, D. B., 2014, "Fusion characteristics of volcanic ash relevant to aviation hazards," Geophys. Res. Lett., 41(7), pp. 2326–2333.

- [8] Hamed, A., Tabakoff, W. C., and Wenglarz, R. A., 2006, "Erosion and Deposition in Turbomachinery," *J. Propuls. Power*, 22(2), pp. 350–360.
- [9] Turner, E. R., Wilson, W. D., Hylton, L. D., Kaufman, R. M., 1985, *Turbine Vane External Heat Transfer, Volume 1. Analytical and Experimental Evaluation of Surface Heat Transfer Distributions with Leading Edge Showerhead Film Cooling*, Indianapolis.
- [10] Hylton, L. D., Nirmalan, V., Sultanian, B. K., and Kaufman, R. M., 1988, *The Effects of Leading Edge and Downstream Turbine Vane Heat Transfer*, Indianapolis.
- [11] Nealy, D. A., Mihelc, M. S., Hylton, L. D., and Gladden, H. J., 1983, "Measurements of heat transfer distribution over the surfaces of highly loaded turbine nozzle guide vanes," *J. Eng. Gas Turbines Power*, 106(January 1984), pp. 149–158.
- [12] Hylton, L. D., Mihelc, M. S., Turner, E. R., Nealy, D. a., and York, R. E., 1983, *Analytical and Experimental Evaluation of the Heat Transfer Distribution over the Surfaces of Turbine Vanes*, Indianapolis.
- [13] Delimont, J. M., Murdock, M. K., Ng, W. F., and Ekkad, S. V., 2015, "Effect of Temperature on Microparticle Rebound Characteristics at Constant Impact Velocity—Part II," *J. Eng. Gas Turbines Power*, 137(11), p. 112604.
- [14] Delimont, J. M., Murdock, M. K., Ng, W. F., and Ekkad, S. V., 2015, "Effect of Temperature on Microparticle Rebound Characteristics at Constant Impact Velocity—Part I," *J. Eng. Gas Turbines Power*, 137(11), p. 112603.
- [15] Boulanger, A., Patel, H., Hutchinson, J., Deshong, W., and Xu, W., 2016, "Preliminary Experimental Investigation of Initial Onset of Sand Deposition in the Turbine Section of Gas Turbines," *ASME Turbo Expo 2016*, Seoul, pp. 1–10.
- [16] Kueppers, U., Cimarelli, C., Hess, K.-U., Taddeucci, J., Wadsworth, F. B., and Dingwell, D. B., 2014, "The thermal stability of Eyjafjallajökull ash versus turbine ingestion test sands," *J. Appl. Volcanol.*, 3(1), p. 4.
- [17] Dunn, M. G., Padova, C., Moller, J. E., and Adams, R. M., 1987, "Performance Deterioration of a Turbofan and a Turbojet Engine Upon Exposure to a Dust Environment," *J. Eng. Gas Turbines Power*, 109(3), p. 336.
- [18] Dunn, M. G., Padova, C., and Adams, M. R., 1987, "Operation of Gas Turbine Engines in Dust-Laden Environments," p. 16.

- [19] Livingood, J. N. B., and Hrycak, P., 1973, Impingement heat transfer from turbulent air jets to flat plates: A literature survey, Washington, D.C., USA.
- [20] Myers, R. H., Montgomery, D. C., and Anderson-Cook, C. M., 2009, Response Surface Methodology: Process and Product Optimization Using Designed Experiments, Wiley.
- [21] Jarvis, E. A. A., and Carter, E. A., 2003, "Exploiting covalency to enhance metal-oxide and oxide-oxide adhesion at heterogeneous interfaces," *J. Am. Ceram. Soc.*, 86(3), pp. 373–386.

3. Conclusion and Future Work

The results obtained from these studies are new and significantly add to the body of literature related to high temperature sand deposition by providing information on how individual sand particles deposit onto simulated engine components. Improving the resilience of gas turbine engines to sand ingestion requires the development of a computational model that will allow for the prediction of sand particle deposition at gas turbine engine representative conditions, and the statistical models from this work are a significant step towards the implementation and validation of that project.

The model developed in the first paper can only explain 65% of the deposition that occurred. Despite the shortcoming, it was a proof-of-concept for the experimental methodology and identified several improvements that could be made to increase the strength of the collected data and resulting model, such as categorizing deposition by surface temperature, controlling sand injection rate, and improving control over gas path temperature. These changes are implemented in the second paper which yielded much more interesting results. The model developed from those experiments is able to explain up to 98.9% of the deposition based on coupon angle and surface temperature. The model shows that deposits increase at a quadratic rate for temperature and angle and that there is an interaction between those two terms. The strength of the collected data and resulting model will allow it to be used to create a useful deposition prediction model, which in turn can be used to model real-world gas turbine engines and components to develop designs that mitigate the effects of sand deposition.

There are several other parameters that can be explored in the future to further the understanding of sand particle deposition in gas turbine engines. The first parameter of interest is to increase the flow temperatures since modern gas turbine engines operate at temperatures up to 1700 °C, which is much higher than the 1100 °C maximum temperature reached in these experiments. As temperatures increase, crystalline sand particles will soften and melt, ultimately altering their collision and deposition properties. For the second parameter, the sponsor wishes to investigate altering the coupon surface temperatures, which would serve as an analogue to cooled turbine hardware. The temperature gradient between the hot gas and sand mixture and the cooled surface could affect how particle adhere to the metal surface. A third factor relates to sand particle impact angle and impact velocity. Currently, impact angle and velocity are estimated using the bulk flow velocity and coupon angle. However, due to flow effects around the coupon surface,

these values may not be representative for every location on the coupon. Particle tracking can be used to locate particles near the coupon and predict their path to the surface, allowing for actual values of angle and velocity to be calculated. A fourth factor is related to the particulate composition and sizing used in this study. The ARD used in the experiments does not accurately simulate airborne sands and dusts from around the world, as the composition of the road dust is dissimilar from the dust typically encountered by jet aircraft. Additionally, the 20-40 μm particulate sizing is not directly representative of sand sizing in the hot section of turbine engines. Particle sizing is typically below 10 μm after the cold sections of a turbine engine since the particles are “pulverized” as they travel through the compressor. Further studies could investigate different particulate compositions and sizing to simulate real-world turbine conditions more accurately.

As discussed in the second paper, particle overlaps were an issue when attempting to characterize deposition at higher temperatures. If testing temperatures are increased, the difficulty identifying distinct particles will increase. To address this issue new methods of measuring deposition could be explored including measuring the mass of the deposited particles or the change in roughness of the coupon surface. Alternatively, the amount of injected particulate could be decreased to reduce the number of sand particles reaching the coupon surface and allowing the current technique to be maintained.

Appendix A: Modifications to the Virginia Tech Aerothermal Rig

To perform safe and effective experiments, several extensive modifications had to be performed to upgrade and improve the test rig. This appendix describes the upgrades performed by the author to improve the Virginia Tech Aerothermal Rig.

A.1. Sand Injector

The sand injector is used to introduce Arizona Road Dust (ARD) to the air stream within the equilibration tube, so it can be heated and accelerated to appropriate conditions before impacting the coupon. To gather usable data the sand must be delivered consistently between tests and the delivery system must allow the rate of sand delivery to be accurately controlled.

The sand injection system used for all tests prior to 2016 is shown in Figure A-1. Before the test the sand is placed in the hopper and the ball valve is opened a set distance using a feeler gauge. To inject the sand, a solenoid valve opens and air is blown down through the hopper forcing the sand-air mixture through the ball valve. A pneumatic agitator is used to ensure that minimal sand remains in the hopper. The hopper system was very inconsistent between tests as the ball valve offered very little control over the sand flow. Additionally, rather than the sand being introduced in uniform concentration throughout the injection period, the initial pulse of air would force a majority of the sand into the rig in a single “slug”.

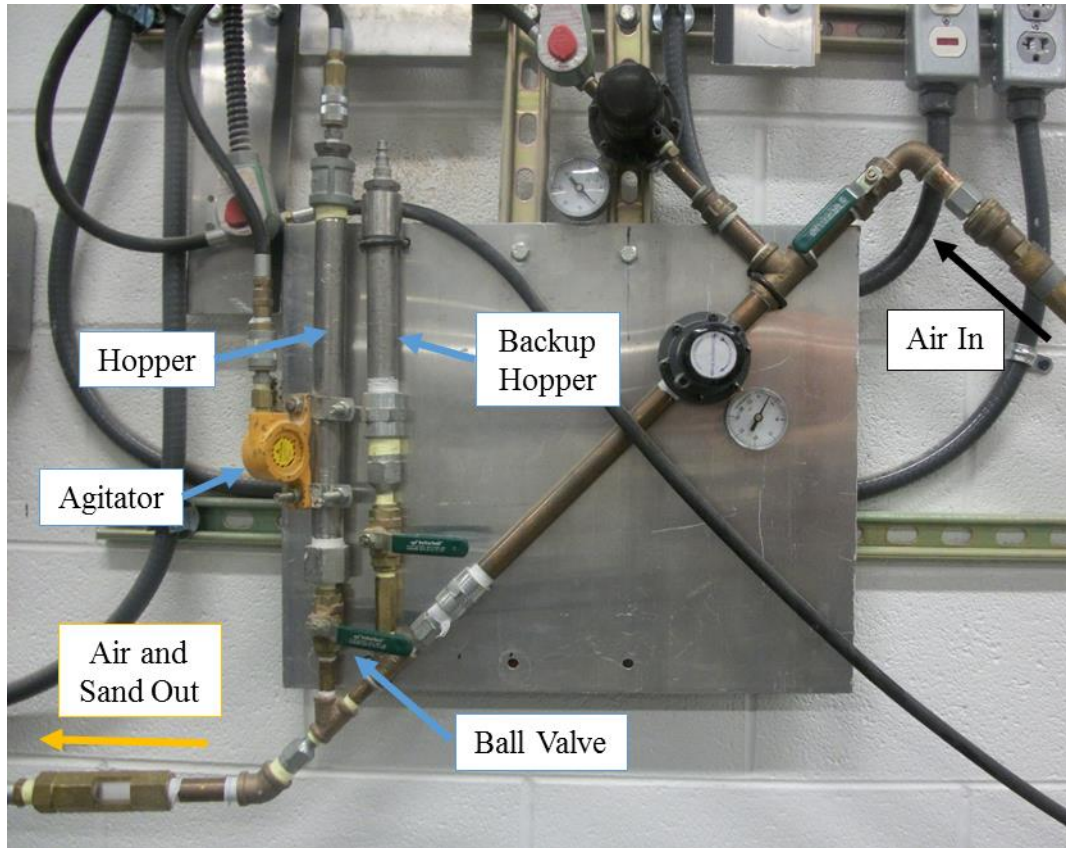


Figure A-1: Previous sand injection system with important components labeled.

To resolve the injection inconsistencies and improve the quality of data, a new sand injection system was designed and built during early 2016. This system, shown in Figure A-2, uses a stepper driven conveyor belt and an air powered vacuum pump. A block diagram illustrating the system operation is included in Figure A-3. A set of adjustable guides is used to ensure that the sand is delivered consistently between tests. Before the test, sand is placed between the guides and smoothed to a uniform height. Desiccant packets are placed within the containment box to prevent the sand from clumping together due to moisture in the air and an air filter is used to prevent contamination. The guides are covered and the containment box is closed to prevent any sand from being lost due to air currents. Next, the air supply is connected to the vacuum pump and adjusted to the appropriate pressure. When the sand is injected, the stepper motor turns the conveyor belt, dropping the sand into the vacuum pump. The speed of the stepper motor can be adjusted by the test operator to change the concentration of the sand being delivered to the coupon. A window was added to the box to monitor the conveyor and ensure that the system is functioning properly.

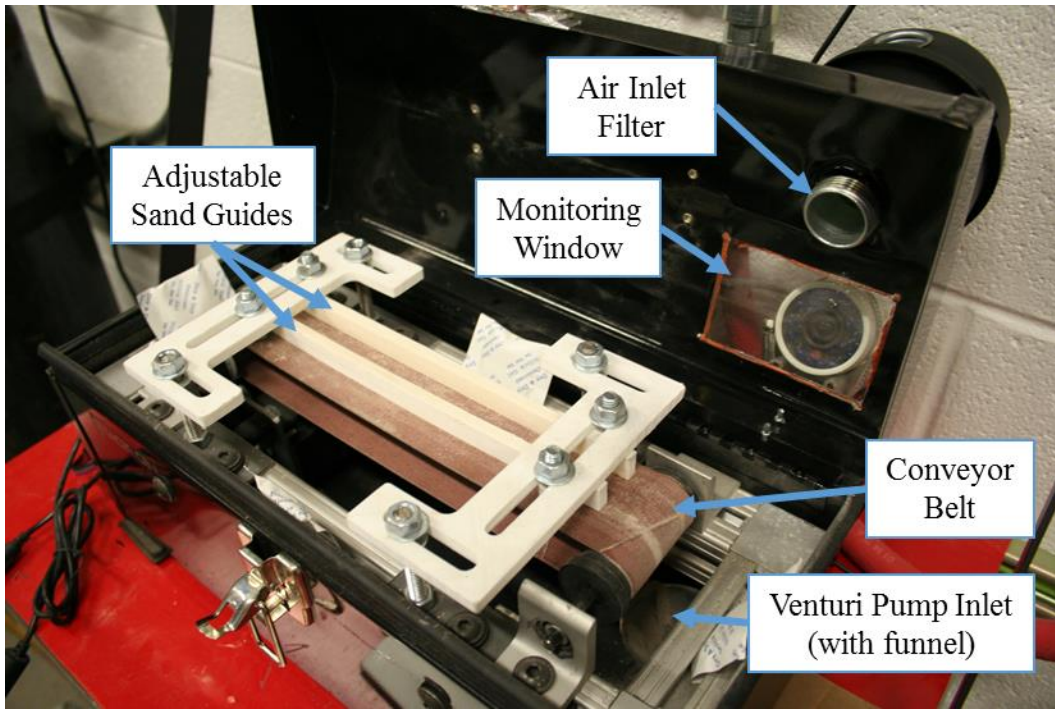


Figure A-2: New sand injection system with important components labeled.

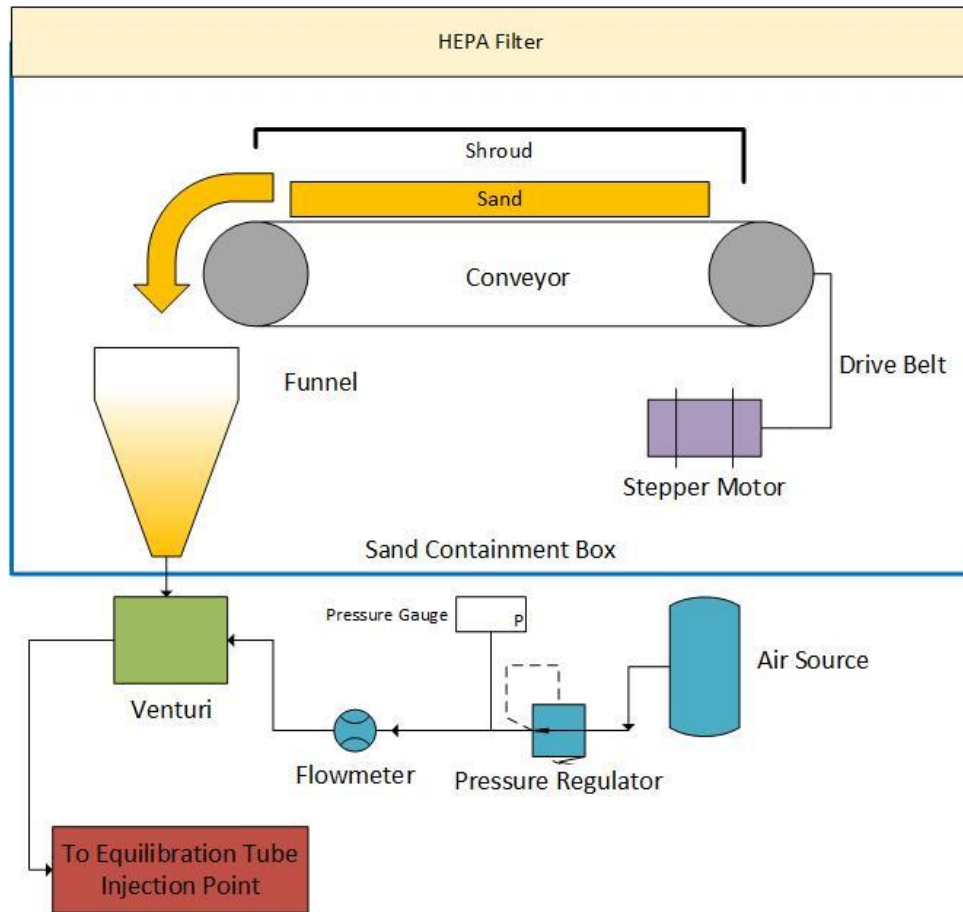


Figure A-3: A block diagram illustrating the operation of the sand injection system

The speed of the conveyor belt was adjusted before testing to ensure a realistic particle concentration of 1000 PPMW was injected. A particle image velocimetry (PIV) system was used to view the sand impacting the coupon and showed that the particulate entered the test section at a uniform rate throughout the injection period. This reduced uncertainty likely contributed to the improved quality of the data between the first and second papers presented in this thesis. This system also allows for the potential to run tests determining the effect of sand concentration on deposition rates as described in the Future Work section.

A.2. Fuel System

The Virginia Tech Aerothermal Rig was originally intended to burn natural gas, which consists primarily of methane, when installed at Virginia Tech. Natural gas lines were not available at the lab space, so the rig was run using laboratory grade compressed methane cylinders instead. These tanks were relatively expensive, needed to be replaced after just a few tests, and required increased

safety precautions to handle and store. Additionally, the expansion of the methane resulted in cooling which could freeze the fuel pressure regulators, resulting in reduced temperature control during extended testing sessions.

To resolve temperature control problems, alternative fuel sources were investigated and propane was chosen as a replacement fuel. Propane is stored as a liquid at lower pressures, which reduces safety risks and eliminates freezing of regulators and valves. Additionally, the tanks are much cheaper and contain more energy per volume than comparable methane tanks, allowing tests to be conducted for a lower cost and reducing the time needed to swap tanks. The new propane system uses three 100 pound tanks connected to a manifold with hoses exiting through a single pressure regulator.

When the Aerothermal Rig was originally installed, the valves and piping were sized to allow for the use of natural gas at much greater volumes than the rig currently requires. As a result, fine adjustments of the amount of fuel entering the burner were extremely difficult. This resulted in poor control over the temperature of the air impacting the test coupon, which could vary ± 20 °C during tests. To improve the control of the fuel flow, new valves were selected and installed. The new system, shown in Figure A-4, uses four electronic needle valves mounted in parallel. These valves were selected due to their high accuracy and their proportional response characteristics. Four valves were needed in order to allow sufficient fuel flow rate to reach the desired testing temperatures. It is possible to install additional valves to the current manifold to increase the fuel flow capacity for higher temperature testing.

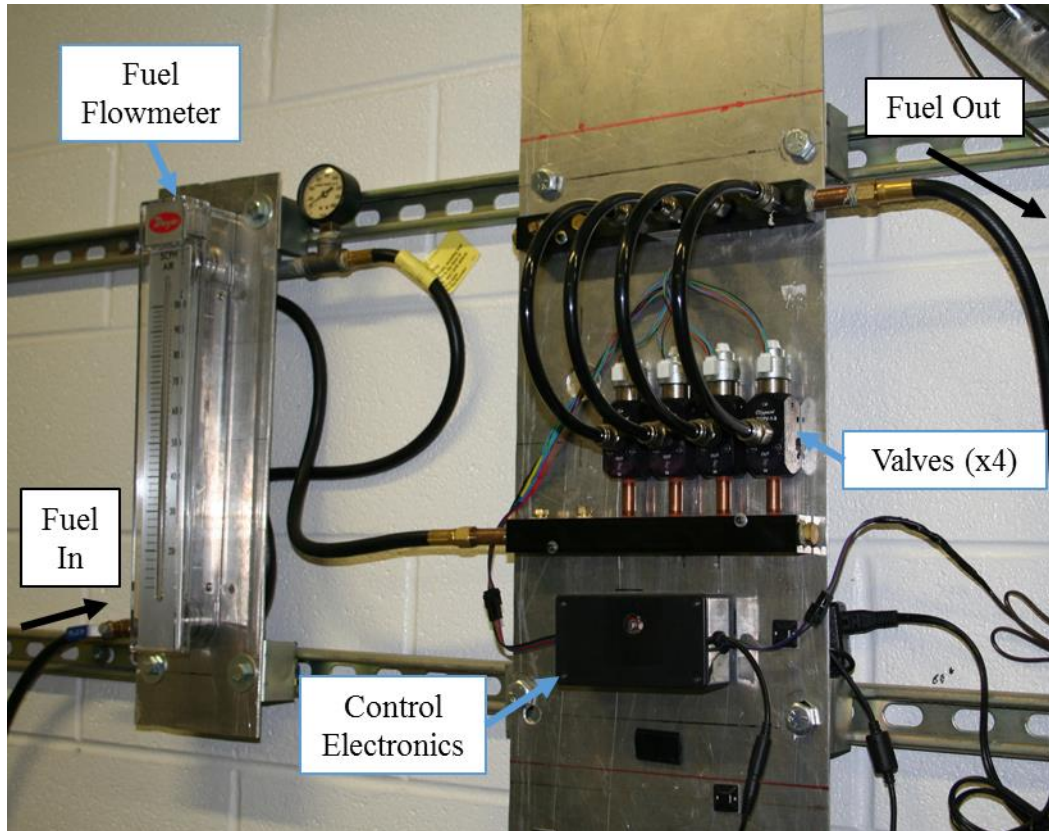


Figure A-4: New fuel control system with important components labeled.

During testing it was found that the Aerothermal Rig with the new fuel configuration could reach 1100 °C, the maximum testing temperature, with the valves approximately 75% open while maintaining that temperature within approximately ± 1 °C. This reduced uncertainty likely contributed to the improved quality of the data between the first and second papers presented in this thesis and will improve the accuracy of future tests utilizing the Virginia Tech Aerothermal Rig.

A.3. Exhaust Quenching

In order to comply with safety and building regulations, the exhaust gasses leaving the Virginia Tech Aerothermal Rig must to be cooled to a safe level. To accomplish this, a water quenching had been previously designed and implemented when the Virginia Tech Aerothermal Rig was first installed. This cooling system required a researcher to enter the test section during testing to turn a valve allowing water to flow to nozzles in the exhaust section, which was a major safety risk. Additionally, if the nozzle was not closed after testing, water could build up in the exhaust and test

section and even back up as far as the equilibration tube, creating the potential for damage to seals and electronic components. To eliminate these issues, an electronic valve was added to the quenching system to allow the water flow to be actuated remotely. A system was added to the control software to automatically turn the quenching flow on and off when the exhaust passed certain temperature limits. An override was also provide to allow the operator to manually activate quenching if required.

A.4. Camera/Laser Containment

Particle image velocimetry (PIV) tests were conducted on the Virginia Tech Aerothermal Rig, using a Dantec Dynamics® FlowSense camera and a Litron Nd:YAG laser. In order to perform tests safely, the laser light needed to be contained within the test section. Ambient light must be blocked to prevent the images from becoming incorrectly saturated. Previous tests used fabric blackout shields for these purposes, but this method was insufficient for containing the laser and was also difficult to set up appropriately. To solve these issues, a new containment system, shown in Figure A-5 was created. This system uses a steel barrel over the camera on top of the test section and a steel bucket over laser lens to the side. The steel barrel uses a cord pass through to allow power and signal wires for the camera to be attached without allowing light to enter or exit. The laser compliance inspector from Virginia Tech Environmental Health and Safety approved the system and indicated that it greatly improved the level of safety for researchers using the laser.

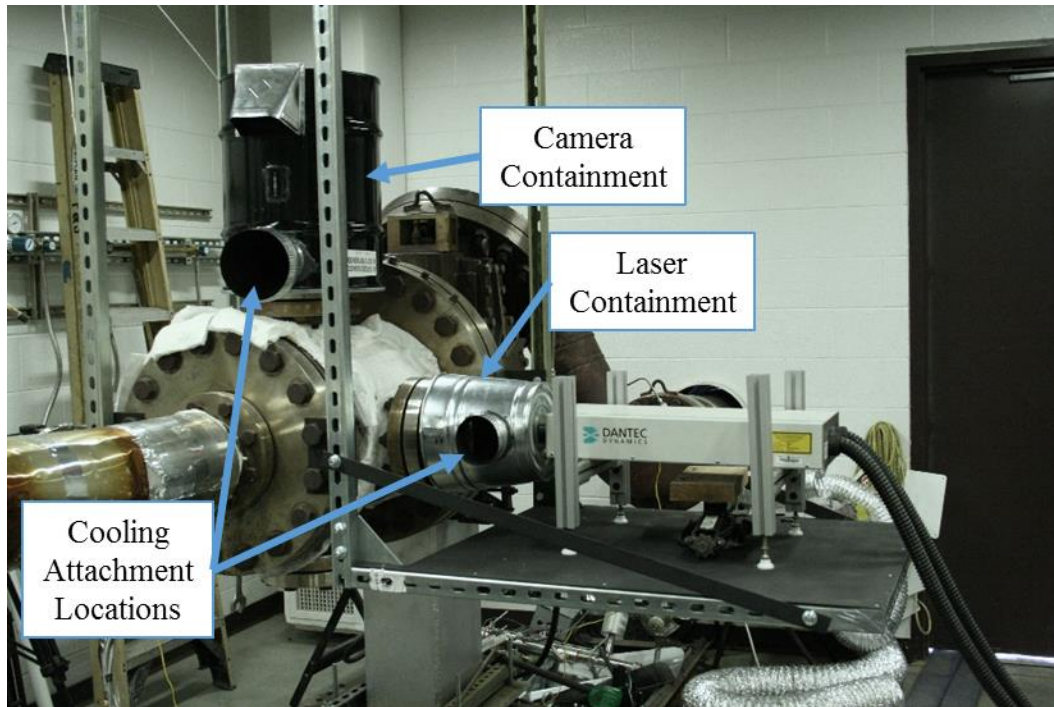


Figure A-5: New camera/laser containment system (cooling hoses removed).

The PIV camera sensor and laser head may suffer damage if heated above 50 °C, so cooling hoses were attached to both containment vessels. The hoses were attached to an ordinary window air conditioning unit to provide cold air. Thermocouples were used to measure the temperatures of the laser and camera so that the test could be shut down if temperatures were to climb to dangerous levels. The cooling was very effective and a shutdown was never necessary during any test and the thermocouples never registered higher than 20 °C at the highest testing temperatures. The improved containment system should improve operator safety and allow for faster test setup when conduction PIV measurements.

A.5. Rig Controls

The Virginia Tech Aerothermal Rig uses two National Instruments CompactDAQs attached to a desktop computer running LabVIEW to control the rig during tests. As the rig was upgraded, more controls and instrumentation were installed, including the new fuel valves, sand conveyor, exhaust quenching, and additional thermocouples for monitoring test coupon and flow temperatures. These controls and indicators were added to the previous version of the control

software. Additionally, the code was completely overhauled to make the software more user-friendly and computationally efficient.

To improve the ease of use of the control software, the Front Panel, shown in Figure A-6, was reorganized to group controls and indicators by their location and function on the rig. This improved the intuitive operation of the rig. Unused controls from previous tests were removed or hidden to streamline the panel. Additionally, high temperature warnings were added, to complement the existing automatic high temperature safety shutdown system.

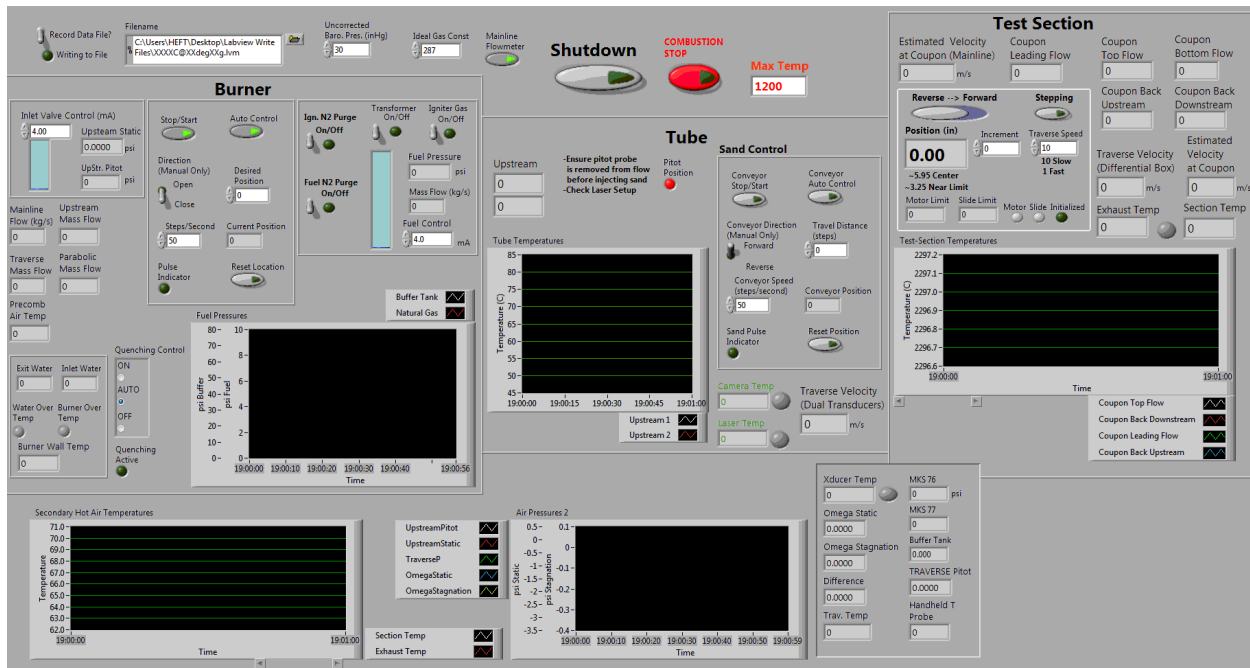


Figure A-6: Front panel of the Aerothermal Rig control software. Controls are organized by Burner, Equilibration Tube, and Test Section.

To accelerate the code execution, it was rewritten to consist of two separate parallel loops, each with its own functionality. The first loop captured data from the cDAQs and wrote it to a buffer. The code for capturing data was improved by using built in LabVIEW functions which speed up acquisition and appropriately scaled the voltage data to proper units. The first loop also performed any calculations required, updated the values on the front panel, and sent control information back to the cDAQ. The second loop copied the buffer data to a file for later analysis. This change prevented timing errors that had occurred previously when trying to perform all operations sequentially, due to the long times it took to write data to the file.

An emergency stop switch was added to the control system that cuts power to the original pneumatic fuel valve controller to stop the burner. An older control computer suffered an unexpected shutdown during a test and it was discovered that under this circumstance, fuel flow would not stop and the Virginia Tech Aerothermal Rig would continue to burn fuel at the rate set prior to the unexpected shut down. To shut down the rig quickly, the fuel tank valves needed to be manually closed from within the test cell, which was a hazard for the operators. Therefore, an emergency shutdown switch removes the hazard for operators during an unexpected control or power loss. In addition, this switch also adds a hardware level safety to prevent the fuel valves from unintentionally being opened from the control program.

Appendix B: Data Reduction Code

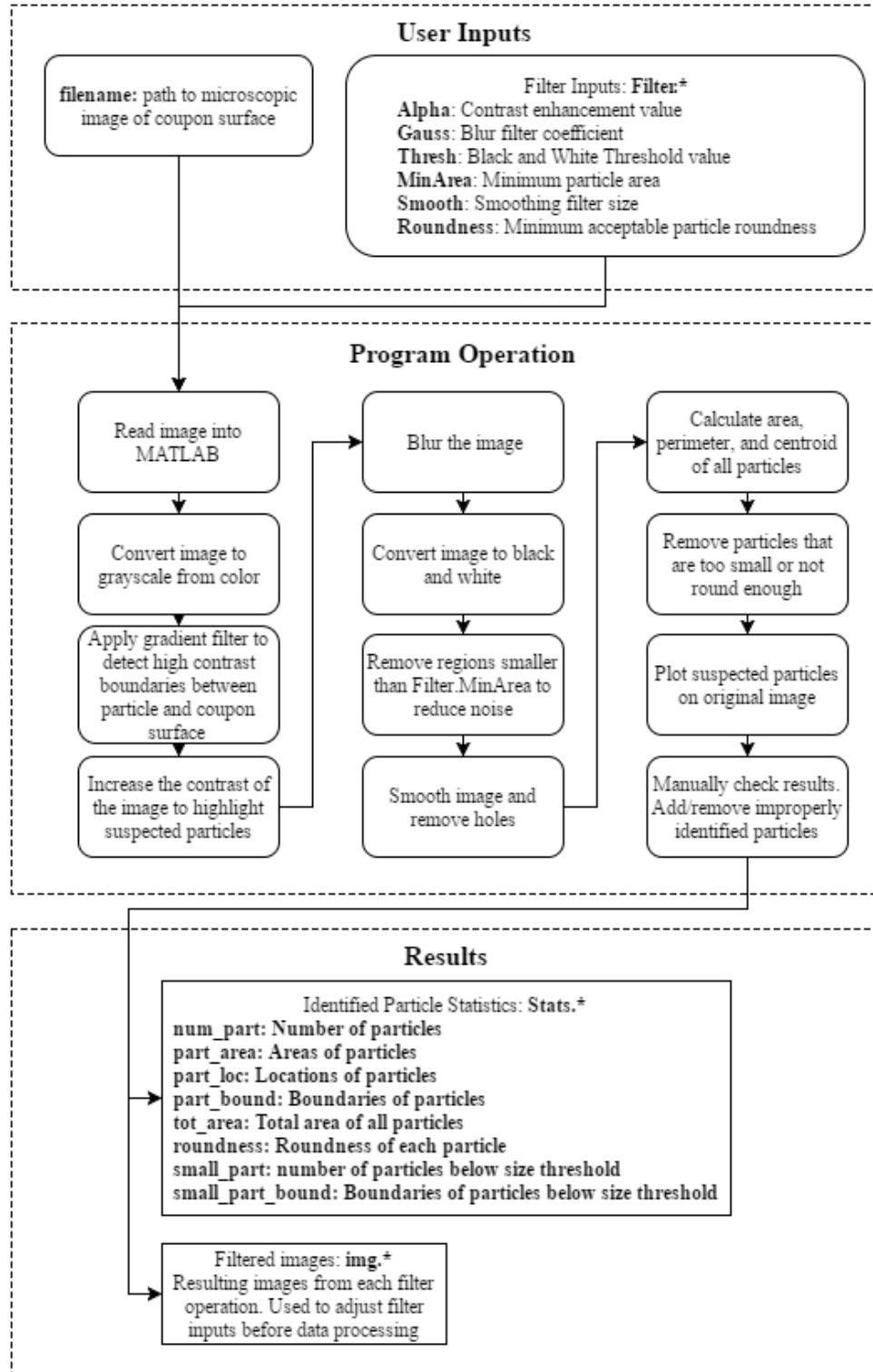
To process microscopic images of the coupon surface into deposition statistics, a new data reduction code was developed. Previous codes had minimal filtering and did not implement built in MATLAB image manipulation functions which resulted in very time intensive post processing. The new code adds these features to improve accuracy and speed, with manual checking of the particle identification, and outputs particle coverage area and particle deposit counts.

First, the code converts the image to grayscale and a gradient filter is applied to the grayscale image. Next, the contrast is increased and a Gaussian blur is applied to find particle regions which appear as shaded regions. The image is converted to black and white and inverted so that particles show up as white spots on a black background. Spots below the minimum particle size are removed and the edges of remaining particles are smoothed and any holes are filled. The area, centroid, and perimeter of any remaining regions is then calculated. The particles are then filtered by size and roundness to remove any noise. The code then enters a manual mode, where any missed particles can be added by the researcher and any false positives can be removed. This code repeats for each image in the dataset and the number of particles and total coverage area in each image is recorded to a file for further analysis. Additionally, a file with filter coefficients, metadata, and individual particle information is saved for future reference.

A block diagram visualizing the operation of the program is included in Section B.1 and the actual code is included in Section B.2.

B.1. Data Reduction Block Diagram

This section contains a block diagram describing the inputs, operation, and outputs of the data reduction code. Bolded text corresponds to program variables.



B.2. Particle_Counter_v18_rev2

```
function [ img, stats ] = Particle_Counter_v18_rev2(filename, filter)
%This function counts deposited particles and coverage area
%on a surface for the Aerothermal Rig deposition testing using texture
%filters
%Doing This function analyzes surface images at varying pixel densities of
% particles using several MATLAB Image Processing Toolbox filters.
%
% Assumptions:
%     1) The image must be focused on the metallic surface of the test
%         specimen
%     2) The image must be a '.bmp' file
%     3) The total number of particle coverage area is underestimated by
%         using the smallest diameter area, to avoid overestimation of
%         coverage, this may change in future meetings with the sponsor
%         (6/11/2015)
%
% Inputs
%     filename: the path where the image(s) are pulled
%
%     filter.[fields]: a structure input containing the following items
%         filter.alpha -> Increase the contrast of the first gray image to
highlight the black
%         spaces where the suspected particles are located. The pixels are
the
%         range from 0 to 255 since the image is still a uint8. The adaptive
%         histogram uses a distribution exponential method with an alpha
value. The
%         alpha value default is 0.4. Recommend starting there and going up
or down
%         accordingly
%
%         filter.thresh -> When converting img.gray3 to black and white,
%         this value sets the threshold (usually 0.9) to convert
%         pixels above that value to white, everything else is converted
%         to black. The range is 0 to 1.
%
%         filter.saltpep -> Integer input. This determines the number of
%         particles that will be filtered out to remove the "salt and
%         pepper" effect from the 2nd black/white image to find the large
%         white areas where the suspected particles will be. A good
%         starting value is 30 pixels.
%
%         filter.smooth -> [pixels pixels]. A good starting point is [15
%         15]
%
%         filter.MinArea -> lower detection limit for the program
%         based on area and perimeter. e.g. if minimum desired area is x,
%         the program will pick up particles x/2.
%
%         filter.roundness -> limit of acceptable roundness for potential
%         detected particles. Provides a good metric to eliminate obscure
%         background shapes that may be detected as particles

x = imread(filename);
```

```

img.org = x;

%% Filter the original image
% the variable 'x' is the working image

% Convert the image to a grayscale from the original
x = rgb2gray(x);
img.gray1 = x;

% Convert the grayscale with a gradient filter
x = imgradient(x);
x = uint8(255*x/max(x(:)));
img.gmag = x;

% Increase the contrast of the first gray image to highlight the black
% spaces where the suspected particles are located. The pixels are the
% range from 0 to 255 since the image is still a uint8. The adaptive
% histogram uses a distribution exponential method with an alpha value. The
% alpha value default is 0.4. Recommend starting there and going up or down
% accordingly
x = adapthisteq(x, ...
    'Distribution', 'exponential', 'Alpha', filter.alpha);
img.gray2 = x;

% blur the image to find particle regions (darker regions)
x = imgaussfilt(x, filter.gauss);
img.blur = x;

% Convert gray3 to black and white with a high threshold to highlight the
% white spaces of the suspected particles
x = imbinarize(x, 'adaptive', 'Sensitivity', filter.thresh);
x = imcomplement(x);
img.bw1 = x;

% Remove the "salt and pepper" effect by removing groups of white pixels
% less than a set number. This is an input, filter.MinArea
x = bwareaopen(x, filter.MinArea);
img.bw2 = x;

% Smooth out the white zone edges and fill the holes
x = medfilt2(x, filter.smooth);
x = imfill(x, 'holes');
img.bw3 = x;

% Find the pixel boundaries of all the white spaces/suspected particles
[stats.bound, region_num] = bwboundaries(x, 'noholes');

% find the attributes of each region, area, centroids, and perimeters (in
% pixels)
stats.prop = regionprops(region_num, 'Area', 'Centroid', 'Perimeter');

% tally the number of particles
stats.num_part = 0;
stats.part_area = [];
stats.part_loc = [];

```

```

stats.part_bound = {};
stats.tot_area = 0;
stats.roundness = [];
small_part = 0;
small_part_bound=[];

%% Automatic Particle Choosing

for i = 1:size(stats.prop,1)

    %calculate the roundness metric of all enclosed particle areas
    stats.roundness(i,1) = 4*pi*stats.prop(i).Area/...
        ((stats.prop(i).Perimeter).^2);

    % conditionals of area and perimeter of each white area to validate
    % particle sizing as well as the roundness
    if stats.prop(i).Area >= filter.MinArea ...
        && stats.roundness(i,1) > filter.roundness

        % particle location in an array that meet the criteria of the
        % conditional
        stats.part_loc(stats.num_part+1, 1) = stats.prop(i).Centroid(1);
        stats.part_loc(stats.num_part+1, 2) = stats.prop(i).Centroid(2);

        % pull the boundaries of the suspected particles
        stats.part_bound{stats.num_part+1,1} = stats.bound{i,1};

        % Add up the total area meeting the conditional criteria (in
        % pixels)
        stats.tot_area = stats.tot_area+stats.prop(i).Area;

        % pull area of suspected particles
        stats.part_area(stats.num_part+1,1) = stats.prop(i).Area;

        % count the number of suspected particles
        stats.num_part = stats.num_part + 1;
    end

    % 90% of the minimum size to filter out any potential particles, ex
    % 9 um if the minimum size is 10 um
    if stats.prop(i).Area < filter.MinArea ...
        && stats.prop(i).Area > 0.9*filter.MinArea ...
        && stats.roundness(i,1) > filter.roundness

        % store the boundary location of the potential particles
        small_part_bound{small_part+1,1}=stats.bound{i,1};

        small_part = small_part+1;
    end
end

%% Plot and Add/Remove Particles

% Plot Particles

```

```

ParticlePlotter();

% plot the particles that might be too small
if isempty(small_part_bound)==0
    hold on;
    for k = 1:length(small_part_bound)
        boundary2 = small_part_bound{k};
        plot(boundary2(:,2),boundary2(:,1), 'r', 'LineWidth',2)
    end
    hold off;
end

% Add or Remove Particles
ParticleAddRemove;

%% Nested Functions (Plotting and Add/Remove Functions)

function ParticlePlotter()
    % Nested Plotting Function
    % plot the original image on the left of the subplot
    clf;
    imshow(img.org, 'Border', 'tight', 'InitialMagnification', 150);
    %montage([img.org, img.org])
    axis on; hold on;
    xlabel('Pixels'); ylabel('Pixels');

%         % draw a line separating the two images
%         X = [size(img.bw3,2)+1 size(img.bw3,2)+1];
%         Y = [0 size(img.bw2,1)];
%         line(X,Y, 'Color', [0 0 0], 'LineWidth', 4);

% plot the boundaries of all suspected particles
for k2 = 1:length(stats.part_bound)
    bound = stats.part_bound{k2};
    plot(bound(:,2), bound(:,1), 'b', 'LineWidth', 2)

    % Numbering the suspected particles
    randRow = ceil(length(bound)/(mod(rand*k2,7)+1));
    col2 = bound(randRow,2);
    row2 = bound(randRow,1);
    h2 = text(col2+1, row2-1, num2str(k2));
    set(h2, 'Color', 'g', 'FontSize', 14, 'FontWeight', 'bold');
end

    hold off

end

function ParticleAddRemove()
    % Select particles for addition or removal:
    % setup a question button to ask if there are particles to remove with
    % the default to be adding if there are no particles to select

    buttonBW = questdlg('Are there particles to add/remove?', 'Add/Remove
Particles?', ...

```

```

        'Remove Particles', 'Add Particles', 'Next Image', 'Add Particles');

loop = 1;
while loop ~= 0

    % Add particles (polygon or elliptical)
    if strcmp(buttonBW, 'Add Particles') == 1
        buttonBW2 = questdlg('Particle Shape? Ellipse or Polygon?', ...
            'Particle Shape', 'Elliptical', 'Polygon', 'Elliptical');

        % Elliptical
        if strcmp(buttonBW2, 'Elliptical') == 1
            % imellipse selects a black/white elliptical mask with the
points
            % associated with each particle
            e = imellipse;
            wait(e);
            BW = createMask(e);
            delete(e);

            % Polygon
        elseif strcmp(buttonBW2, 'Polygon') == 1
            % roipoly selects a black/white image mask with the points
            % associated with each particle
            BW = roipoly;
        end

        % Check if mask exists to prevent crashes
        if sum(sum(BW)) > 0

            % determine the region properties of the mask
            tempAddPart = regionprops(BW, 'Area', 'Centroid',
'Perimeter');

            % conditionals of area and perimeter of each white area to
validate
            % particle sizing
            if tempAddPart.Area > filter.MinArea

                % Store the boundary of the particle
                tempAddPartBound = bwboundaries(BW, 'noholes');

                % Plot the new particle boundary
                plot(tempAddPartBound{1,1}(:,2),
tempAddPartBound{1,1}(:,1), ...
                    'r', 'LineWidth', 2);

                % Append new particle to statistics values
                stats.bound = [stats.bound; tempAddPartBound];
                stats.prop = [stats.prop; tempAddPart];
                stats.num_part = stats.num_part+1;
                stats.part_area = [stats.part_area; tempAddPart.Area];
                stats.part_loc = [stats.part_loc;
tempAddPart.Centroid];
            end
        end
    end
end

```

```

stats.part_bound = [stats.part_bound;
tempAddPartBound];
stats.tot_area = stats.tot_area + tempAddPart.Area;
stats.roundness = [stats.roundness; 0];

% Replot the new particle and retally
ParticlePlotter();

else
% If particle does not meet minimum size requirements
uiwait(msgbox({'...
'Selected particle does not meet size
requirements',...
' ',...
['Size is ' num2str(tempAddPart.Area,4) ' pixels
(~'...
num2str(0.27*sqrt(4*(tempAddPart.Area)./pi()),4) '
micron)']},...
'ERROR!', 'error','modal'));
%(0.27 um/pixel ratio from microscope with 20x
% magnification), Diameter assumes round particles
end
else
% Mask selection error (if it is a line or point)
uiwait(msgbox('Mask selection error! Please try again.',...
'ERROR!', 'error','modal'));
end
end

% Removes particles potential
if strcmp(buttonBW, 'Remove Particles') == 1 ...
&& isempty(stats.part_loc)==0

% remove particle from list
x = inputdlg('Enter particle index (single particle only):',...
'Remove Particle', 1);
data = floor(str2double(x));

if isempty(data) == 0
if data<=stats.num_part && data>0
stats.num_part = stats.num_part-1;
stats.part_loc(data, :) = [];
stats.part_bound(data,:) = [];
stats.tot_area = stats.tot_area -
stats.part_area(data);
stats.part_area(data) = [];
else
uiwait(msgbox('Particle index outside of range! Please
try again.',...
'ERROR!', 'error','modal'));
end
end
% Plot the new particles without the previous one
ParticlePlotter();

end

```

```
% Go to next image
if strcmp(buttonBW, 'Next Image') == 1
    break
end

    buttonBW = questdlg('Are there particles to add/remove?',
'Add/Remove Particles?',...
    'Remove Particles','Add Particles','Next Image','Add
Particles');

    end

end

end
```

Appendix C: Non-Dimensionalization

In order to gain further understanding into the physics behind onset of sand particle deposition, it was desirable to form a dimensionless representation of the experimental data. Since only two terms, coupon near-surface temperature and coupon angle, were tested during the previous experiment, the complexity of the dimensionless model is limited to those terms as independent variables. These variables and other important constants along with their respective fundamental units are included in. Additional dimensional analysis is provided in Section C.1 which predicts which terms may be of interest for future deposition studies.

Table C-1: Measured variables and other important constants along with their respective symbol and fundamental units

Important/Measurable Factors	Symbol	Units
Deposits (particles/mm ²)	D_p	$1/L^2$
<i>Near Surface Temperature</i>	T_{NS}	Q
<i>Flow Temperature</i>	T_∞	Q
Sintering Temperature	T_{sint}	Q
Flow Velocity	V_∞	L/T
<i>Normal Velocity (function of angle)</i>	V_n	L/T
Particle Concentration (PPMW)	PPMW	[]
Particle Diameter	d_p	L

Italics indicate factors varied during experiment

*_p refers to particle properties

*_s refers to coupon surface properties

*_∞ refers to flow properties

- 1) Select repeated variables from Table C-1 which capture all 3 fundamental units (length, temperature, and time)

$$d_p, V_\infty, T_\infty \rightarrow L^2Q/T$$

2) Non-dimensionalize remaining variables using combinations of repeated variables

$$D_p \rightarrow \pi_1 = \frac{D_p \pi d_p^2}{4}$$

$$T_s \rightarrow \pi_2 = \frac{T_{NS}}{T_{sint}}$$

$$V_n \rightarrow \pi_3 = \frac{V_n}{V_\infty} = \frac{V_\infty \sin\theta}{V_\infty} = \sin\theta$$

3) Develop function from non-dimensionalized terms:

$$\frac{D_p \pi d_p^2}{4} = \text{Coverage Percent} = f\left(\frac{T_{NS}}{T_{sint}}, \sin\theta\right)$$

4) Determine function coefficients from experimental data:

$$D_{CP} = 2619.6 - 5959.6 T^* - 518.68 \theta^* + 568.05 T^* \theta^* + 3397.6 T^{*2} + 35.334 \theta^{*2}$$

$$\text{where } T^* = \frac{T_{NS}}{T_{sint}} \text{ and } \theta^* = \sin(\theta)$$

C.1. Theoretical Model

This section describes the creation of a more complete dimensionless equation for sand deposition which provides a prediction on what factors should be tested in the future to provide a more complete analysis of the physical mechanisms.

From the experiment, we would like to develop equation of the form:

$$\frac{D_p \pi d_p^2}{4} = \text{Coverage Percent} = \text{Sand Amount} * \text{Capture Efficiency} * \text{Sticking Ratio}$$

1. Sand Amount: The sand amount describes a ratio of the projected area of sand particulate per unit area of air. This is based off of the sand concentration and the densities of sand and air.

$$s = \left(\frac{PPMW}{10^6} \frac{\rho_\infty}{\rho_p} \right)^{\frac{2}{3}} \quad (\text{Sand concentration per unit area})$$

$$\rho_\infty = f(T_\infty, P_\infty, R_\infty) \quad (\text{Exhaust gas density from ideal gas law})$$

$$\text{Therefore, } s = f(PPMW, \rho_p, T_\infty, P_\infty, R_\infty)$$

2. Capture Efficiency: The capture efficiency describes a ratio of particles striking the coupon surface to the total amount of injected particles. This ratio is primarily a factor of Stokes number, a non-dimensional quantity which describes the behavior of particles suspended in a fluid flow. This ratio is to be determined by CFD analysis of the experimental setup and may be validated through PIV measurements.

$$\text{Of the form } \eta_{cap} = \frac{Stk^2}{(Stk + C_1)^2} \text{ with } C_1 \text{ determined empirically from CFD simulations}$$

$$Stk = \frac{t_\infty V_\infty}{l_c} \text{ where } t_\infty = \frac{\rho_p d_p^2}{18 \mu_\infty} \text{ and } \mu_\infty = \frac{1.458 \times 10^{-6} \frac{kg}{m \cdot s} K^{0.5} T_\infty^{\frac{3}{2}}}{T_\infty + 110.4 K} \quad (\text{Sutherland Relation for Air})$$

$$\text{Therefore, } \eta_{cap} = f(V_\infty, l_c, \rho_p, d_p, T_\infty)$$

3. Sticking ratio: The sticking ratio describes a ratio of particles sticking to the coupon surface to the total amount of particles hitting the surface. It is theorized that this ratio is a relation between the kinetic energy of an approaching particle and energy released upon impact and deformation of the particle and coupon surface, but this relationship needs to be confirmed by experimental observations.

$$\eta_{stick} = \frac{DE}{KE} \text{ where } KE = \frac{2}{3} \rho_p \pi d_p^3 V_n^2 \text{ and}$$

$$DE = \int \text{Deformation Force} = \frac{8}{15} E^* \left(\frac{d_p}{2} \right)^{1/2} \text{depth}^{5/2}$$

$$\text{where } E^* = \frac{1-v_p^2}{E_p} + \frac{1-v_s^2}{E_s} \text{ and } E_x = f(T_x) \text{ and depth is to be analytically determined by}$$

analyzing the deformation and contact area of particles seen in coupon images

Therefore, $\eta_{stick} = f(\rho_p, d_p, V_n, \nu_p, \nu_s)$

Total equation combining previous quantities:

$$\text{Coverage Percent} = f(\text{PPMW}, \rho_p, T_\infty, T_s, P_\infty, R_\infty, V_\infty, V_n, l_c, d_p, \nu_p, \nu_s)$$

Removing Constants ($\rho_p, P_\infty, R_\infty, l_c, \nu_p, \nu_s$):

$$\text{Coverage Percent} = f(\text{PPMW}, T_\infty, T_s, V_\infty, V_n, d_p) \text{ where } V_n = f(V_\infty, \theta)$$

Current experiments have determined effect of T_∞ , T_s , and θ . Therefore, tests must be performed on the remaining variables, PPMW, V_∞ , and d_p , in order to determine the effects of and develop coefficients for those terms. Furthermore, empirical relations for Young's Modulus of the sand particles and coupon surface, $E_x=f(T_x)$, must be located or measured.